Lateral-distortional buckling of steel-concrete composite beams: kinematics, GBT constrained modes and analytical formulae

Heitor F. Araujo[1], Carlos M. Andrade Jr.[2], Cilmar Basaglia[3], Dinar Camotim[4]

Abstract

This paper investigates the kinematics and mechanics involved in the lateral-distortional buckling (LDB) behavior in I-section steel beams elastically restrained by concrete slabs (involving web single or double curvature), and uses the findings obtained to develop and illustrate the application of analytical formulae to calculate LDB moments of steel-concrete composite beams. The study is based on a Generalized Beam Theory (GBT) approach to perform buckling analyses that is based on constrained deformation modes, which incorporate the displacement/rotation restraints due to the slab, thus making it possible to obtain accurate buckling results with only a few deformation modes. The solution of the equilibrium equation for the LDB of simply supported I-section steel beams, restrained by a concrete slab and under uniform negative (hogging) bending, is derived analytically in the context of the above GBT formulation. In order to illustrate the capabilities and potential of the derived formulae, several buckling moments are determined, discussed and compared with values calculated by other formulae available in the literature. For validation and assessment purposes, the results obtained are also compared with values provided by conventional GBT, finite strip and/or ANSYS shell finite element analyses.

1. Introduction

Steel-concrete composite beams are extensively used in the building construction industry – their structural advantages are well known and stem from the fact that combine a steel profile (often I-section) and a concrete slab working together, due to use of shear connectors at the steel-concrete interface – see Fig. 1(a). The influence of the concrete slab on the steel I-section beams are commonly simulated by means of longitudinally continuous (i) full or partial rotational restraints and (ii) full lateral restraints at the level of the beam (connected) top flange – the former is modelled by an elastic spring with stiffness k_r (*e.g.*, Bradford 1998 and Goltermann & Svensson 1988), as shown in Fig. 1(b). The value of k_r is usually obtained from either experimental tests, numerical simulations or equations based on simplified structural models (*e.g.*, Calenzani *et al.* 2012, Johnson & Fan 1991) – the latter approach is adopted in the current European Standard (CEN 2004).

---

[1] FECFAU, Department of Structural Engineering, University of Campinas, Brazil. < heitordfaraujo@gmail.com>
[2] FECFAU, Department of Structural Engineering, University of Campinas, Brazil. < carlosmagalhaes.eng@gmail.com>
[3] FECFAU, Department of Structural Engineering, University of Campinas, Brazil. <cbasaglia@fec.unicamp.br>
[4] CERIS, DECivil, Instituto Superior Técnico, Universidade de Lisboa, Portugal. <dcamotim@ist.utl.pt>
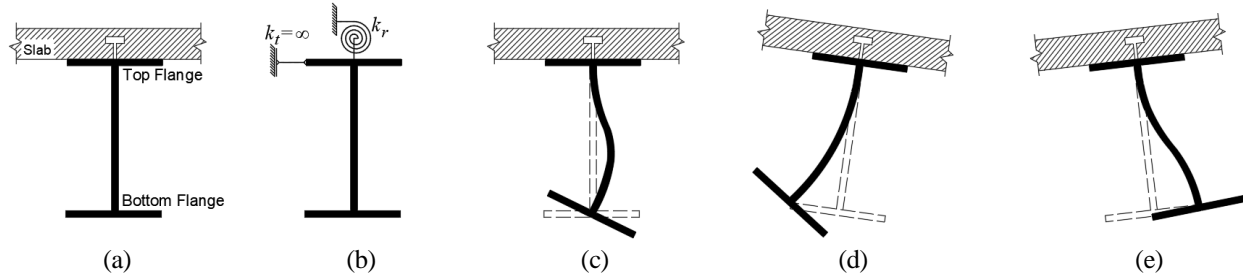
Figure 1: (a) Steel-concrete composite beam, (b) longitudinally continuous spring modelling the rotational restraint provided by the slab, (c) web local buckling and (d) single and (e) web double curvature lateral-distortional buckling

While the concrete slab provides full restraint against lateral-torsional buckling to the I-section beam spans under positive (sagging) bending moments, the same is not true for the regions under negative (hogging) bending moments. In the latter, buckling may occur in either a web local mode, illustrated in Fig. 1(c), or a lateral-distortional mode, combining (i) a lateral motion of the (unrestrained) compressed flange and (ii) web transverse bending in single or double curvature, as shown in Figs. 1(d)-(e) (*e.g.*, Bradford 1992, Silvestre 2010). The possible occurrence of lateral-distortional buckling stems from the (partial) restraint provided by the concrete slab to the I-section, responsible for changing the buckling mode nature from lateral-torsional to lateral-distortional.

Since the 1980s, several investigations were devoted to the development of numerical methods and simplified formulations to determine the lateral-distortional buckling (LDB) behavior of I-section steel beams restrained by concrete slab – among them, it is worth noting the works of (i) Bradford (1986, 1988a,b) who developed energy-based models and one-dimensional finite element formulations, (ii) Hanswille *et al.* (1998), Zhou *et al.* (2016) and Dias *et al.* (2019), who proposed calculation procedures to estimate the critical LDB moments, (iii) Zhou and Yan (2017), who used refined non-linear finite element models capable of accounting for various effects influencing the composite beam behavior, such as initial geometrical imperfections, residual stresses or the interface slip, and (iv) Gonçalves & Camotim (2010) and Henriques *et al.* (2016, 2020), who developed an enhanced finite element based on Generalized Beam Theory (GBT) to handle shear lag, concrete cracking and shear connection flexibility effects.

Concerning the approaches to estimate LDB moments of I-section steel beams restrained by concrete slabs, it is worth mentioning that Hanswille *et al.* (1998) and Dias *et al.* (2019) proposed energy methods based on the well-known inverted U-frame model, which account for the concrete slab in the calculation of the rotational spring stiffness – however, this model is limited to web single curvature LDB. On the other hand, Zhou *et al.* (2016) proposed a methodology that can also handle web double curvature LDB – nevertheless, it was derived under the assumption of null rotation of the (connected) top flange, *i.e.*, an infinite torsional stiffness provided by the concrete slab.

It is still worth noting that consensus has not yet been reached concerning the kinematics and mechanics underlying LDB – indeed, there are discrepancies between the critical moments LDB yielded by the various approaches. These discrepancies stem from the different kinematic assumptions adopted by each approach (*e.g.*, Rossi et al. 2020). Therefore, it is fair to argue say that the kinematics and mechanics of this instability phenomenon in elastically restrained I-section beams are not yet fully understood. This explains (at least partially) why the analytical formulae available concern almost exclusively web transverse bending in single curvature web and fully fixed (connected) top flanges (*e.g.*, Silvestre 2010).

Mechanical models based on conventional GBT, taking advantage of its unique modal features, have been successfully employed (i) to acquire deep insight on the distortional buckling behavior of unrestrained cold-formed steel members with open "unbranched" cross-sections, namely, zed-section, lipped channel and rack-section members, and also (ii) to develop analytical and semi-analytical formulae to determine approximate (but accurate) distortional buckling loads and moments of such members (e.g., Silvestre & Camotim 2004a,b,c). Very recently, the authors extended the domain of application of the above approach to derive analytical and semi-analytical buckling formulae for restrained zed-section and lipped channel members (Araujo *et al.* 2021). This extension required the direct incorporation of the restraints in the conventional GBT cross-section analysis (procedure leading to the determination of the deformation modes and associated modal mechanical properties) – the output of the ensuing "modified GBT cross-section analysis" was a set of constrained deformation modes reflecting accurately the mechanics of the restrained member under scrutiny, thus making it possible to obtain accurate buckling results with only a few (often one or two) deformation modes. In order to further extend the domain of application of the above approach, so that it can handle the LDB kinematics and mechanics in I-section steel beams restrained by concrete slabs, it is indispensable to incorporate the restraints provided by slab directly in the GBT cross-section analysis of open "branched" cross-sections (such as the I-section) – recall that the previous works dealt exclusively with members with open "unbranched" cross-sections.

Therefore, the purpose of this work is to use a modified/improved GBT-based approach to shed fresh light on the kinematics and mechanics of (web) single and double curvature LDB in I-section steel beams restrained by concrete slabs, namely by identifying the cross-section properties relevant for this buckling phenomenon. Moreover, the GBT constrained deformation modes incorporating the displacement/rotation restraints due to the slabs are employed to derive approximate (but accurate) analytical formulae to calculate LDB moments. Several numerical examples are presented to illustrate the application and assess the performance of these formulae, namely by comparing the LDB moments they provide with those either yielded by other formulae available in the literature or obtained from shell finite element analyses (SFEA).

The outline of the paper is as follows. First, the main concepts and numerical procedures involved in determining the GBT constrained deformation modes of open "branched" cross-sections are presented in Section 2. Then, Section 3 addresses the main mechanical features of single and double curvature LDB in elastically restrained I-sections, and also presents and discusses the kinematical assumptions generally adopted in the context of this buckling phenomenon – these assumptions are used to develop a simple procedure to build the web flexural and lateral displacement fields of elastically restrained I-sections. Next, in Section 4, the modified GBT formulation is used to derive and analytically solve the LDB equilibrium equation for simply supported I-section steel beams restrained by concrete slabs under uniform hogging bending moments – moreover, a set of LDB moments provided by the derived analytical formulae are presented, discussed and compared with values obtained from other formulae available in the literature. For validation and assessment purposes, the LDB moments determined in this work are also compared with values either yielded by the programs GBTUL2.0 (Bebiano *et al.* 2018, conventional GBT) and CUFSM (Li & Schafer 2010, Finite Strip Method – FSM), or obtained by ANSYS SFEA (SAS 2013). The paper closes, in Section 5, with a few concluding remarks.

It should be noted that, in the derivations and equations presented throughout the paper, (i) all scalar quantities, including the matrix components, are denoted by *italic letters*, (ii) a virtual

3

variation is denoted by δ, (iii) tensor notation is employed, (iv) a subscript preceded by a comma indicates differentiation (*e.g.*, $(\cdot)_{,x} \equiv d(.)/dx$) and (v) Einstein's summation convention is adopted. Matrix and vector components are identified by square ([ ]) and curly ({ }) brackets, respectively – however, when specifying components is not necessary, matrices and vectors are identified by **normal bold** and *italic bold* symbols, respectively.

2. Proposed GBT Approach

Consider the arbitrary prismatic thin-walled open cross-section member schematically displayed in Fig. 2, which is deemed (i) formed by *n* walls (plate elements), each divided into various segments with width b_i, and (ii) restrained by continuous translational (normal and tangential – stiffness values K_{TN} and K_{TG}, respectively) and rotational (stiffness K_R) elastic springs located at arbitrary points S_P. Also shown in Fig. 2 are the wall/local coordinate axes *x*, *s* and *z*, respectively along the member axis, cross-section mid-line and wall thickness (*t*). In order to obtain a displacement field representation compatible with the classical beam theory, each displacement component $u(x, s)$, $v(x, s)$ and $w(x, s)$ at any given cross-section mid-line point must be expressed as a combination of orthogonal functions. Therefore, one has

$$u(x,s) = u_i(s)\varphi_{i,x}(x) \qquad\qquad v(x,s) = v_i(s)\varphi_i(x) \qquad\qquad w(x,s) = w_i(s)\varphi_i(x) \qquad , \ (1)$$

where (i) $u_i(s)$, $v_i(s)$, $w_i(s)$ are shape functions used to approximate the cross-section displacement field and (ii) $\varphi_i(x)$ are non-dimensional amplitude functions defined along the member length – information on the derivation of these expressions can be found in the works of Schardt (1989) and Silvestre & Camotim (2002).

The equations providing the member buckling behavior, taking into account the presence of elastic constraints (springs), are obtained by imposing the stationarity of the total potential energy functional

$$V = \frac{1}{2}\int_{\Omega} \sigma_{ij}\varepsilon_{ij}d\Omega + \frac{1}{2}\int_{L} K\Delta_r^2 dx \qquad\qquad (2)$$

in the close vicinity of the member fundamental equilibrium path (adjacent equilibrium). Note that (i) Ω is the member volume (*n* walls), (ii) σ_{ij} and ε_{ij} are the second Piola-Kirchhoff stress and Green-Lagrange strain tensors, respectively, both including pre-buckling and bifurcated components, (iii) *L* is the member length, (iv) *K* is the stiffness of a longitudinally distributed continuous (along an axis *r*) spring and (v) Δ is the corresponding spring generalized displacement (translation or rotation) – the summation convention applies to subscripts *i* and *j*. Then, the equilibrium equations defining the member buckling eigenvalue problem are obtained by (i) linearising the first variation of the total
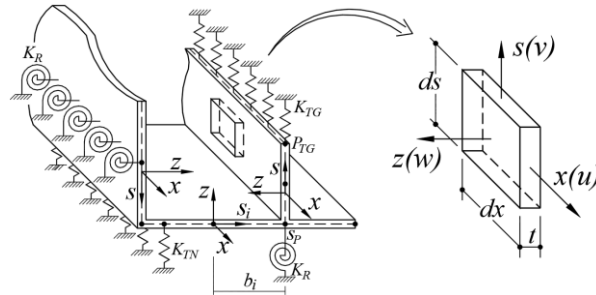
Figure 2: Arbitrary continuously restrained open-section thin-walled member and wall/local coordinate axes

potential energy functional, at the fundamental equilibrium path, and (ii) discarding the pre-buckling strains, thus yielding

$$\delta V = \int_L \left(\begin{array}{c} \delta\boldsymbol{\varphi}_{,xx}^{\mathrm{T}}\mathbf{C}\boldsymbol{\varphi}_{,xx} + \delta\boldsymbol{\varphi}^{\mathrm{T}}\mathbf{B}\boldsymbol{\varphi} + \delta\boldsymbol{\varphi}_{,x}^{\mathrm{T}}\mathbf{D}\boldsymbol{\varphi}_{,x} + \\ \delta\boldsymbol{\varphi}_{,xx}^{\mathrm{T}}\mathbf{E}\boldsymbol{\varphi} + \delta\boldsymbol{\varphi}^{\mathrm{T}}\mathbf{E}\boldsymbol{\varphi}_{k,xx} + \lambda W_j^0 \delta\boldsymbol{\varphi}_{,x}^{\mathrm{T}}\mathbf{X}_j \delta\boldsymbol{\varphi}_{,x} \end{array} \right) dx = 0 \qquad , \quad (3)$$

with

$$\mathbf{B} = \mathbf{B}^{\mathrm{f}} + \mathbf{B}^{\mathrm{s}} \qquad , \quad (4)$$

where (i) λ is the load parameter, (ii) $\boldsymbol{\varphi}$ is a vector containing the longitudinal amplitude functions of the cross-section shape functions, (iii) W_j^0 is a vector whose components are the normal stress resultant profiles associated with uniform internal forces and bending moments j, (iv) $\mathbf{B}^{\mathrm{s}}$ is a matrix associated with the elastic strain energy stored in the translational and rotational springs, (v) $\mathbf{X}_j$ is a geometric stiffness matrix associated with the pre-buckling longitudinal normal stresses and (vi) $\mathbf{C}$, $\mathbf{B}^{\mathrm{f}}$, $\mathbf{D}$ and $\mathbf{E}$ are linear stiffness matrices, associated with several cross-section mechanical properties, namely (vi$_1$) primary/secondary warping, (vi$_2$) transverse extension/flexure, (vi$_3$) plate shear distortion/torsion and (vi$_4$) membrane/flexural Poisson effects – the various matrix components are given by the expressions

$$C_{ik} = C_{ik}^M + C_{ik}^F = Et\int_b u_i u_k \, ds + \frac{Et^3}{12(1-\upsilon^2)}\int_b w_i w_k \, ds \qquad (5)$$

$$B_{ik}^{\mathrm{f}} = B_{ik}^M + B_{ik}^F = \frac{Et}{1-\upsilon^2}\int_b v_{i,s} v_{k,s} \, ds + \frac{Et^3}{12(1-\upsilon^2)}\int_b w_{i,ss} w_{k,ss} \, ds \qquad (6)$$

$$D_{ik} = D_{ik}^M + D_{ik}^F = \int_b Gt(u_{i,s}+v_i)(u_{k,s}+v_k)\, ds + \int_b \frac{Gt^3}{3} w_{i,s} w_{k,s} \, ds \qquad (7)$$

$$E_{ik} = E_{ik}^M + E_{ik}^F = \int_b \frac{\upsilon Et}{1-\upsilon^2} u_i v_{k,s} \, ds + \int_b \frac{\upsilon Et^3}{12(1-\upsilon^2)} w_i w_{k,ss} \, ds \qquad (8)$$

$$X_{jik} = \frac{Et}{C_{jj}}\int_b u_j(v_i v_k + w_i w_k)\, ds \qquad , \quad (9)$$

with C_{jj} related to W_j^0 by means of

$$W_j^0 = C_{jj}\varphi_{j,xx}^0 \qquad , \quad (10)$$

where (i) superscripts $(\ )^M$ and $(\ )^F$ denote membrane and flexural terms, (ii) E, υ and G are the steel Young's modulus, Poisson's ratio and shear modulus, (vi) b is the cross-section mid-line overall width and (vii) $u_j\varphi_{j,xx}^0$ stands for the pre-buckling axial displacement field.

The presence of elastic constraints is taken into account through matrix $\mathbf{B}^{\mathrm{s}}$, which is given by

$$\mathbf{B}^{\mathrm{s}} = \sum_{\gamma=0}^{\eta_{TN}} \mathbf{w}^{\mathrm{T}}(s_P)\mathbf{K}_{\mathbf{TN}}^{\gamma}\mathbf{w}(s_P) + \sum_{\gamma=0}^{\eta_{TG}} \mathbf{v}^{\mathrm{T}}(s_P)\mathbf{K}_{\mathbf{TG}}^{\gamma}\mathbf{v}(s_P) + \sum_{\gamma=0}^{\eta_{R}} \mathbf{w}_{,s}^{\mathrm{T}}(s_P)\mathbf{K}_{\mathbf{R}}^{\gamma}\mathbf{w}_{,s}(s_P) \qquad , \quad (11)$$

where (i) matrices $\mathbf{v}(S_P)$, $\mathbf{w}(S_P)$ and $\mathbf{w}_{,s}(S_P)$ contain the transverse membrane and flexural displacements and flexural rotations at point S_P, where the displacement/rotation restraint γ is located ($S_P = s_i(s_P)/b_i$), (ii) $\mathbf{K_{TN}}$, $\mathbf{K_{TG}}$ and $\mathbf{K_R}$ are diagonal matrices whose non-null components correspond to the translational and rotational spring stiffness values of the restrained wall segments (K_{TN}, K_{TG}, K_R), (iii) η_{TN}, η_{TG} and η_R are the total numbers of translational (normal and tangential) and rotational springs. Since, in Eq. (11), the generalized forces associated with springs are calculated by means of the shape functions, this approach is more accurate than that recently proposed by Araujo *et al.* (2021), who adopted wall segment in-plane rigid-body translations and rotations to determine $\mathbf{B^s}$.

Because the cross-section displacement field is expressed as a linear combination of structurally meaningful deformation modes, GBT analyses involve solving equilibrium equation systems written in a very convenient modal form, which leads to solutions providing in-depth insight on the member structural response under consideration. The performance of a buckling analysis of a restrained member involves (i) a (modified) *cross-section analysis*, to obtain the constrained deformation modes and corresponding mechanical properties, and (ii) a *member analysis*, *i.e.*, the solution of the buckling eigenvalue problem followed by the (modal) interpretation of the results determined (critical loads and buckling mode shapes).

2.1 Cross-section Analysis

Although the conventional cross-section analysis (no restraints) is by now trivial (*e.g.*, Schardt 1989, Silvestre & Camotim 2002, Dinis *et al.* 2006, Bebiano et al. 2015), its extension to restrained members with open cross-sections exhibiting branching nodes (those dealt with in this work, namely I-section steel beams restrained by concrete slabs) poses some difficulty. In order to overcome this difficulty, one must (i) identify and separate the node-based elementary deformation mode families of the unrestrained cross-section, which constitute the building blocks for the determination of the final (structurally meaningful) deformation modes, as proposed by Bebiano *et al.* (2015), (ii) incorporate the restraints (elastic springs) in matrix $\mathbf{B}$, which stems from wall bending, and (iii) determine and characterize the constrained deformation modes, as described by Araujo *et al.* (2021)[5].

The cross-section analysis procedure starts with a cross-section discretization involving natural and intermediate nodes. While the former are mandatory and located at all wall mid-line intersections and free edges, the later are discretionary (intended to refine the cross-section discretization) and located within the wall mid-lines (subdividing the walls into wall segments). Four degrees of freedom (three associated with the translations along the x, s and z axes, and one rotation about the x axis) are assigned to each node, and an initial deformation mode basis is generated by using (i) linear functions for the displacements along x and y, and (ii) cubic Hermite polynomials for the displacements along z. This procedure, whose concepts and operations are described and illustrated in detail by Bebiano *et al.* (2015), subdivides the whole deformation mode set into various subsets (or "families"), according to the nature of the deformations involved. Initially, elementary deformation modes, associated with the imposition of single unit nodal DOFs, are determined, using the appropriate shape functions mentioned earlier and viewing the cross-section as an adequately restrained plane frame model. These elementary deformation modes must be combined and organized according to their distinct

---

[5] The choice of the procedure developed by Bebiano *et al.* (2015) is due to the fact that it (i) can be numerically implemented in a systematic and straightforward fashion, and (ii) provides a rational set of *elementary deformation modes* hierarchically organized into several families, each exhibiting well defined mechanical characteristics.

mechanical natures, which are directly related to the particular combination of node and imposed unit displacement/rotation types – namely (i) *Vlasov* modes (deformation modes complying with Vlasov's assumptions of null membrane shear strains and transverse extensions), (ii) *Shear* modes (non-Vlasov deformation modes with null transverse extensions) and (iii) *Transverse Extension* modes (non-Vlasov deformation modes with membrane transverse extensions).

Once the cross-section shape functions ($u_i(s)$, $v_i(s)$ and $w_i(s)$) of the elementary deformation modes that satisfy Vlasov's hypothesis are known[6], it becomes possible to calculate matrices **B**, **C**, **D** (linear matrices) and $\mathbf{X}_1$ (geometric matrix associated with uniform compression)[7] – recall that the elastic strain energy stored in the springs is accounted for by matrix $\mathbf{B^s}$ (Eqs. (4) and (11)). Fully populated matrices (highly coupled equilibrium equations) are obtained, whose components have no obvious/clear structural meaning.

Lastly, as done for the identification of the cross-section deformation modes (final shape functions), $\bar{u}_k(s)$, $\bar{v}_k(s)$, $\bar{w}_k(s)$, and for the calculation of the associated cross-section modal mechanical and geometrical properties ($\bar{C}_{ik}$, $\bar{B}_{ik}$, $\bar{D}_{ik}$, $\bar{E}_{ik}$, $\bar{X}_{jik}$), the methodology adopted in this work is that recently proposed by Araujo *et al.* (2021) for restrained cross-sections. It requires (i) solving one, two or three auxiliary eigenvalue problems, involving matrices **B**, **C**, **D** and $\mathbf{X}_1$ (all calculated with the shape functions of the Vlasov's elementary deformation modes) and (ii) performing "cross-section rotation analysis procedures" for some eigenvectors obtained from the first auxiliary eigenvalue problem – recall that the conventional GBT cross-section analysis procedure (*e.g.*, Schardt 1989, Silvestre & Camotim 2002, Dinis *et al.* 2006, Bebiano et al. 2015) involves solving three auxiliary eigenvalue problems whose eigenvectors are the standard/unconstrained deformation modes.

In order to illustrate the unique features of the procedure described, consider the steel (*E=200GPa* and *υ=0.3*) branched open cross-section shown in Fig. 3(a) – its dimensions and GBT discretization are also depicted. For the discretization shown, the GBT cross-section analysis leads to set of 18 deformation modes. As for Fig. 3(b), it provides the unrestrained (**R0**) and restrained (**R1** and **R2**) cross-sections, as well as the spring stiffness values. For each of them, Fig. 4 (i) shows the in-plane shapes of the first eight deformation modes and (ii) provide the corresponding $\bar{C}_{kk}$, $\bar{B}_{kk}$, $\bar{D}_{kk}$ and $\bar{E}_{kk}$ (diagonal) matrix components – the observation of the results displayed in this figure leads to the following remarks:

(i) It is possible to assess very clearly the influence of the constraints on the deformation mode shapes and corresponding mechanical properties.

(ii) The $\bar{B}_{kk}$ values concerning the constrained rigid-body deformation modes are either null (like their unconstrained counterparts) or positive, depending on whether they involve or not spring deformations. For instance, $\bar{B}_{22}$ of cross-section **R1** and $\bar{B}_{44}$ of cross-section **R2** stem from the elastic strain energy stored in the translational and rotational springs, respectively.

---

[6] Note that the initial shape functions are determined before the elastic restraints are taken into account, which involves a simple and well-known numerical implementation that requires a low computational effort.

[7] Naturally, it is also possible to include the elementary shear and transverse extension deformation modes and calculate the mechanical properties of these modes for the restrained cross-sections. However, since their cross-section analysis is more complex and these deformation modes do not come into play in buckling analysis of members subjected to uniform internal forces and moments (*i.e.*, they have no bearing on the work reported in this paper), it was decided to consider here only the Vlasov's modes (see, for instance, Basaglia & Camotim 2013 and Bebiano et al. 2015). Restrained members under arbitrary loadings will be addressed in the future.
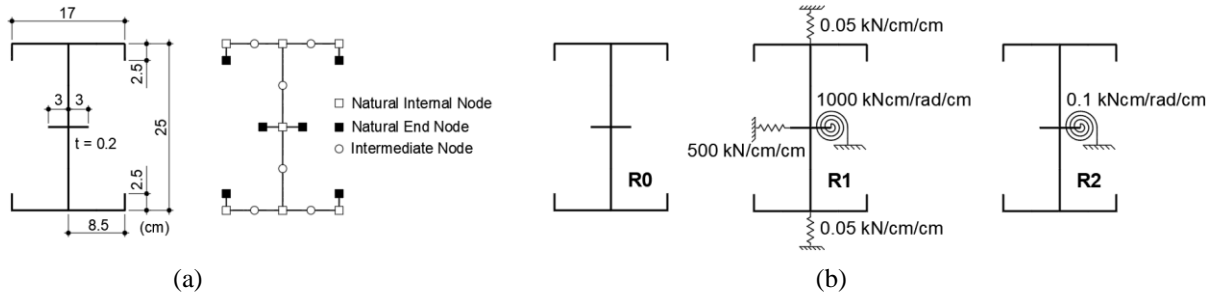
Figure 3: (a) Cross-section mid-line dimensions and GBT discretisation, and (b) schematic representations of the unrestrained (**R0**) and restrained (**R1** and **R2**) cross-sections

R0

	2x2	3x3	4x4	5x5	6x6	7x7	8x8	9x9
$\bar{C}_{kk}$	3.1532E+07	6.2378E+06	1.0796E+09	9.4538E+04	4.6585E+04	4.6585E+04	4.6585E+04	4.6585E+04
$\bar{B}_{kk}$	0.0000	0.0000	0.0000	0.0279	0.0687	0.1646	0.1776	0.1799
$\bar{D}_{kk}$	0.0002	0.0000	1566.3137	13.4723	12.5510	8.1880	11.1413	11.2855
$\bar{E}_{kk}$	0.0000	0.0000	0.0000	-0.4850	-0.0039	-0.1788	0.3855	0.4217

R1

	2x2	3x3	4x4	5x5	6x6	7x7	8x8	9x9
$\bar{C}_{kk}$	3.1532E+07	3.3410E+06	3.1705E+06	4.5602E+04	4.5479E+04	4.5479E+04	4.5479E+04	4.5479E+04
$\bar{B}_{kk}$	0.1000	0.0211	0.0233	0.0870	0.0912	0.1734	0.1756	314.9730
$\bar{D}_{kk}$	0.0000	8.3651	8.7177	11.8739	11.8465	10.8770	11.0178	10.1815
$\bar{E}_{kk}$	0.0000	0.1118	0.1235	0.1206	0.1405	0.3764	0.4117	-1.8882

R2

	2x2	3x3	4x4	5x5	6x6	7x7	8x8	9x9
$\bar{C}_{kk}$	3.1532E+07	6.2378E+06	1.0942E+09	9.4538E+04	4.6582E+04	4.6582E+04	4.6582E+04	4.6582E+04
$\bar{B}_{kk}$	0.0000	0.0000	0.1000	0.0279	0.0689	0.1646	0.1776	0.1799
$\bar{D}_{kk}$	0.0000	0.0000	1566.9788	13.4723	12.5402	8.1876	11.1407	11.2848
$\bar{E}_{kk}$	0.0000	0.0000	1.2423	-0.4850	-0.0021	-0.1788	0.3855	0.4217

Figure 4: Eight most relevant deformation modes and their components $\bar{C}_{kk}$, $\bar{B}_{kk}$, $\bar{D}_{kk}$ and $\bar{E}_{kk}$ for the unrestrained (**R0**) and restrained (**R1** and **R1**) cross-sections – dimensions in *cm*, Young and shear moduli in *kN/cm²*

(iii) Because cross-section **R1** contains constraints that partially restrain torsion and minor-axis bending, its deformation modes **3** and **4** (global deformation modes in unconstrained cross-sections) deformation combine global, distortional and local deformations.

(iv) While the cross-section **R2** constraints do not restrain major and minor-axis bending (modes **2** and **3**) and torsion (mode **4** on an elastic foundation), the cross-section **R1** constraint only does not restrain major-axis bending (mode **2** on an elastic foundation) – thus, C_{22}, C_{33} and D_{44} are practically identical for cross-sections **R0** and **R2**, and C_{22} is equal for cross-sections **R0** and **R1**.

2.2 Member Analysis

After performing the cross-section analysis, one obtains the member GBT system of adjacent equilibrium equations, which (i) is expressed in modal form as

$$\bar{C}_{ik}\bar{\varphi}_{k,xxxx} + (\bar{D}_{ik} - \bar{E}_{ki} - \bar{E}_{ik})\bar{\varphi}_{k,xx} + \bar{B}_{ik}\bar{\varphi}_k - \lambda \bar{X}_{jik}\left(\bar{W}_j^0 \bar{\varphi}_{k,x}\right)_{,x} = 0 \qquad (12)$$

and, together with the adequate end support conditions, (ii) defines the buckling eigenvalue problem to be solved. It is worth mentioning that all the GBT buckling results presented in this paper concern simply supported members (end cross-sections locally/globally pinned and able to warp freely) and were obtained through the application of Galerkin's method with sinusoidal approximation functions (as done in Araujo *et al.* 2021). In order to be able to perform this same task for members with arbitrary support conditions, it is necessary to resort to GBT-based beam finite elements, such as that developed in Silvestre & Camotim (2003).

One of the main features of GBT-based buckling analysis is the possibility of obtaining modal participation diagrams, which enable the assessment and quantification of the contributions of each deformation mode to the member buckling modes. It should be noted that the participation factor of deformation mode *k* to a member buckling mode is obtained as the ratio between (i) the strain energy associated with the contribution of this deformation mode and (ii) the sum of such strain energies associated with all the deformation modes participating in the buckling mode – this is the approach adopted in the program GBTUL (Bebiano *et al.* 2018). In previous works (*e.g.*, Camotim & Basaglia 2013), the participation factor of deformation mode *k* was obtained as the ratio between (i) the area under the $\left|\bar{\varphi}_k(x)\right|$ plot and (ii) the sum of such areas under the plots concerning all the deformation modes participating in the buckling mode.

In order to validate and illustrate the application and potential of the GBT-base buckling analysis based on constrained deformation modes, numerical results are presented and discussed next. They concern the buckling behavior of an uniformly compressed column and a beam subjected to hogging bending moments, both (ii) exhibiting the branched open cross-section whose geometry, dimensions and GBT discretization are given in Fig. 3(a), (iii) made of steel ($E=200GPa$ and $\upsilon=0.3$) and (iv) with pinned end sections that can warp freely – while the column is restrained by constraint **R3**, the beam is braced by constraint **R4** (see Fig. 5(a). The validation of the GBT-based buckling results (critical buckling loadings and mode shapes) is made through the comparison with values yielded by the programs GBTUL2.0 (conventional GBT, Bebiano *et al.* 2018) and CUFSM (Finite Strip Method, Li & Schafer 2010). Note that program GBTUL 2.0 performs standard cross-section analyses (no restraints considered), which means that the deformation modes determined concern the unrestrained member cross-section –

the influence of the restraints (elastic springs) is incorporated only at the member analysis stage (as constraint equations – see Camotim *et al.* 2008).

For the **R3** and **R4** restrained cross-sections, Fig. 5 (b) displays the 9 first constrained deformation modes obtained by means of the proposed cross-section analysis procedure (mode **1** stands for axial extension) – for comparison purposes, note that Fig. 4 depicted the (conventional) deformation modes of the unrestrained cross-section **R0**. Using a single half-wave sinusoidal function to approximate the mode amplitude functions $\bar{\varphi}_k(x)$ and performing buckling analyses for a wide range of lengths (L) leads to the column and beam signature curves shown in Figs. 6 and 7, respectively. These curves provide the variation of the critical buckling load (P_{cr}) and moment (M_{cr}) with the member length L (logarithmic scale), concerning the unrestrained (dashed curve) and restrained (solid curves) members, which can be compared with values yielded by the programs GBTUL (solid circles) and CUFSM (symbols +). The local minima of the signature curves correspond to critical loads/moments associated with either local, distortional or lateral-distortional buckling (no local minimum exists associated with global buckling). Figs. 6 and 7 also show member modal participation diagrams, based on both the constrained (top) and unconstrained (bottom) deformation modes. Concerning these buckling results, it is worth pointing out that:

(i)   First of all, the buckling loads and moments yielded by the FSM and the two GBT buckling analyses (including all deformation modes) virtually coincide – all differences are below 2.8%.

(ii) The signature curves of the restrained members exhibit local minima corresponding to critical buckling loads/moments associated with local (**L**), distortional (**D**) and lateral-distortional (LD) modes, (i) at $L_L{=}11\,cm$, $L_D{=}129\,cm$ and $L_{LD}{=}683\,cm$, for the column, and (ii) at $L_L{=}9\,cm$, $L_D{=}101\,cm$ and $L_{LD}{=}574\,cm$, for the beam.

(iii) While the local minima concerning **L** and **D** buckling virtually coincide for the unrestrained and restrained members (column and beam), those concerning **LD** buckling mode do not occur in
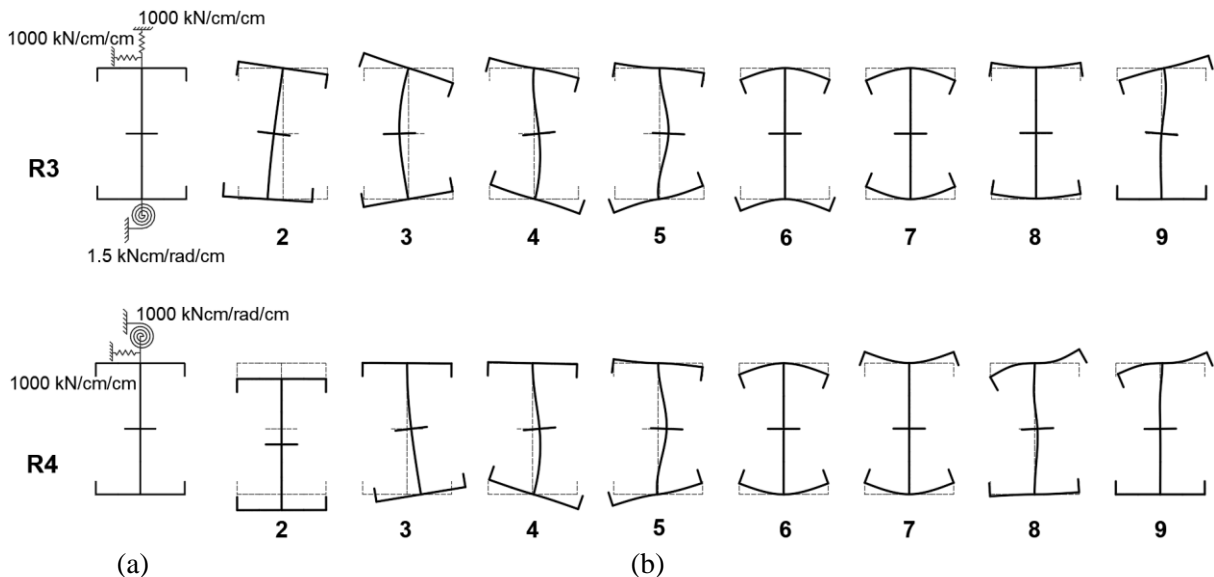
Figure 5: (a) Schematic representations of the restrained **R3** and **R4** cross-sections and (b) configurations of the corresponding 9 first constrained deformation modes

the unrestrained members – in the column and beam, constraints **R3** and **R4** change the buckling mode nature from lateral-flexural (**LF**) and lateral-torsional (**LT**) to lateral-distortional.

(iv) The **L** (both members) and **D** (beam) buckling behaviours are not affected by the restraints. On the other hand, constraint **R3** provides restraint against distortional buckling in the column – in fact, the distortional critical buckling load increases by about 30%.

(v) The modal participation diagrams shown in Figs. 10 and 11 readily show that the constrained deformed modes are much more efficient than their unconstrained/conventional counterparts in assessing the column and beam buckling behaviours. Indeed, it is possible to obtain accurate member buckling results by including in the GBT buckling analyses just one or two constrained deformation modes, regardless of whether buckling occurs in distortional or lateral-distortional modes.
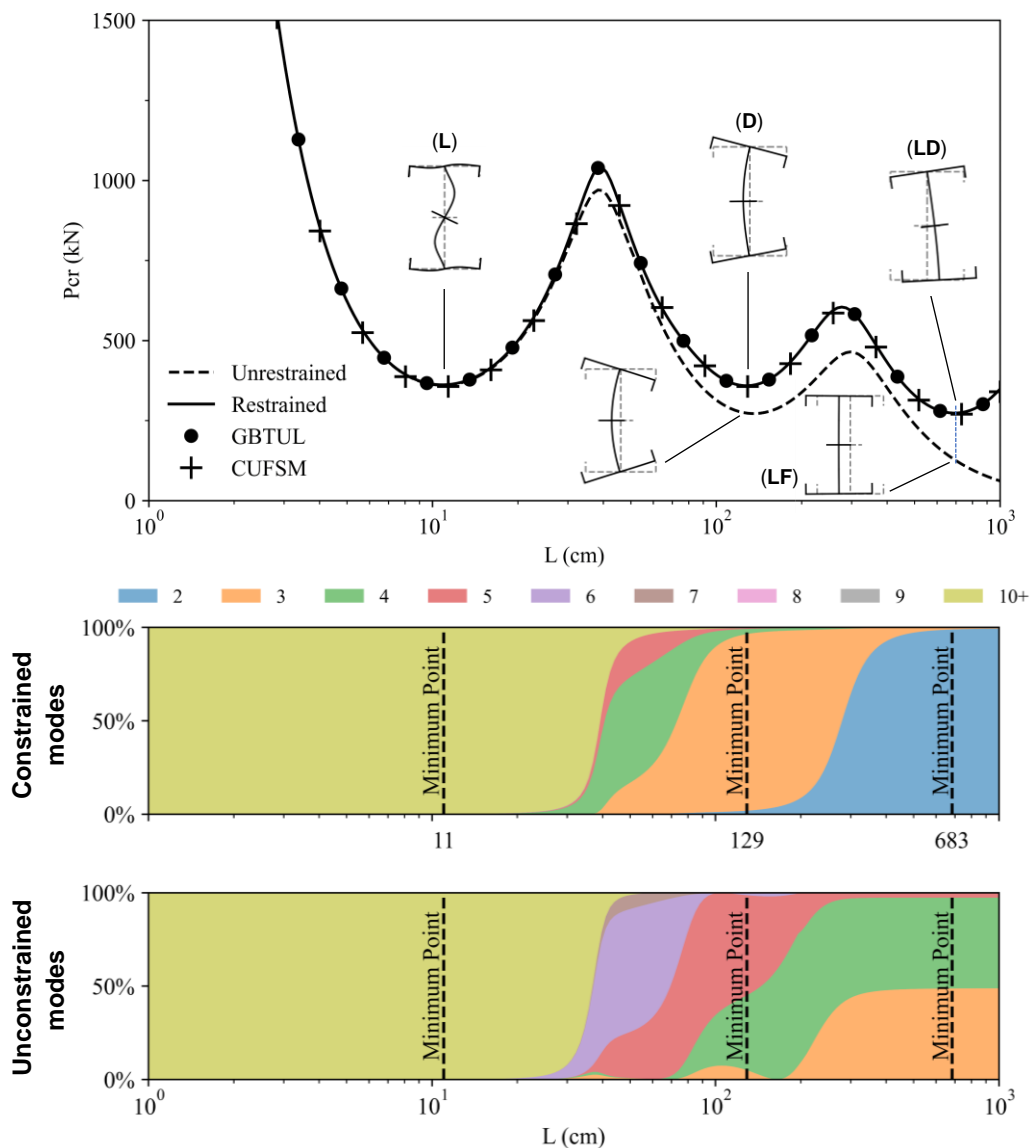
Figure 6: Signature curves P_{cr} vs. L of columns **R0** and **R3**, modal participation diagrams of column **R3**, based on constrained and unconstrained GBT deformation modes, and critical buckling mode shapes.

11
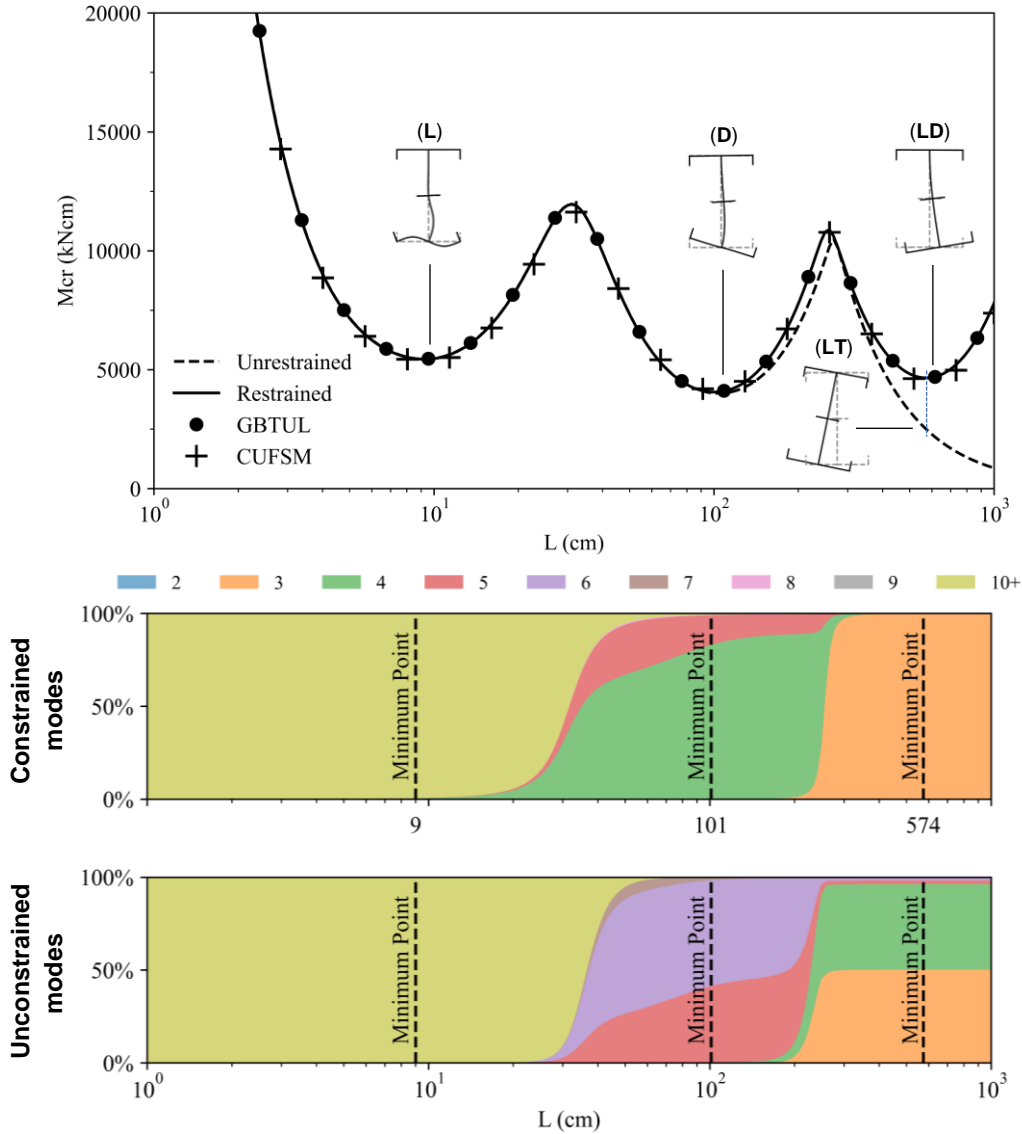
Figure 7: Signature curves M_{cr} vs. L of beams **R0** and **R4,** modal participation diagrams of beam **R4**, based on constrained and unconstrained deformation modes, and critical buckling mode shapes.

3. Restrained I-sections: GBT-Based Buckling Analysis and Kinematics

Although the current Eurocode 4 (CEN 2004) does not prescribe any expression to determine elastic LDB moments (M_{cr}) of steel-concrete composite beams, it recommends their calculation on the basis of the so-called "inverted U-frame" mechanism, consisting of two or more parallel steel profiles plus the overlapping concrete slab (*e.g.*, CEN 2004). In this case, as shown in Fig. 8, the buckling behaviour of the I-section steel member is influenced by the slab flexural stiffness (related to rotation θ_1), shear connection flexibility (related to rotation θ_3) and, especially, web bending (related to displacement δ_2). Since routine design approaches require simple procedures, the current European specification includes a simplified model of the U-frame mechanism: an elastically restrained I-section steel beam with the diaphragm restraints and rotational stiffness, provided by the concrete slab to the steel member, comprising continuous translational (k_t) and rotational (k_r) springs at the top flange-web corner (see Fig. 1(b)). As described in Dietrich *et al.* (2019), it is assumed that the slab fully restrains the

12
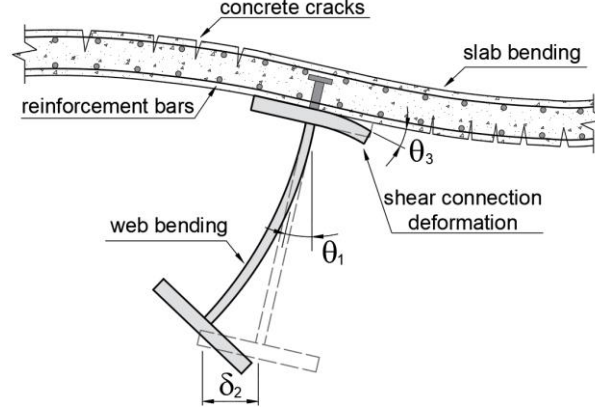
Figure 8: Deformations associated with lateral-distortional buckling

top flange lateral displacement (*i.e.*, $k_t = \infty$), whereas k_r is the joint stiffness of three springs connected in series and representing the cracked concrete flexural stiffness (k_1), steel web flexural stiffness (k_2) and shear connection stiffness (k_3) – Eurocode 4 (CEN 2004) neglects the last one in sections with plane unstiffened webs (k_3 is much higher than k_1 and k_2) (Amaral *et al.* 2018). Therefore, the steel beam rotational stiffness k_r per unit length is given by the expression

$$ k_r = \left(\frac{1}{k_1} + \frac{1}{k_2} \right)^{-1} . \quad (13) $$

3.1 GBT-based Buckling Analysis

In the context of GBT-based buckling analysis of steel-concrete composite beams using the simplified model previously mentioned (with springs), the web deformation is already taken into account by the formulation unique modal features − the rotational stiffness k_r, taken as the concrete slab flexural stiffness (k_1), is obtained from

$$ k_r = k_1 = \frac{\alpha (EI)_{cs}}{a} , \quad (14) $$

where (i) α is a coefficient accounting for the position of the beam in the floor system, (ii) $(EI)_{cs}$ is the cracked flexural stiffness per unit width of the concrete slab and (iii) a is the spacing between parallel beams.

When the steel-concrete composite beam is under hogging bending moments, the concrete slab is acted by tensile stresses and, therefore, must be deemed cracked − its strength stems only from the steel rebars. The presence of the steel rebars (with total area A_s) under tension shifts the cracked cross-section neutral axis from the I-section centroid to a position closer to the slab (G_c), the increasing the web compressed width and reducing the bottom flange compressive stress. Neglecting shear lag effects and shear connection slip, the elastic longitudinal normal stress distribution acting on the composite beam steel I-section can be recovered by adding uniform compressive stresses to the stresses acting on the isolated steel cross-section of the simplified model (instead of considering the steel rebars), as shown Fig. 9 (*e.g.*, Calenzani 2012, Hanswille *et al.* 1998, Dias *et al.* 2019, Amaral *et al.* 2018). Therefore, to achieve the pre-buckling stress equivalence in the simplified method adopted in the constrained-mode GBT analysis considered in this work,
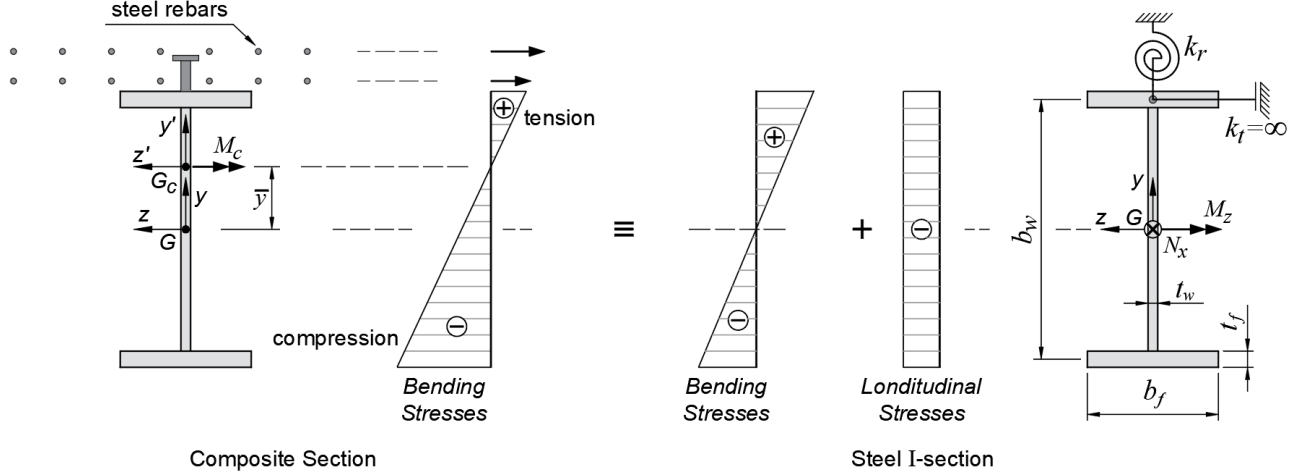
Figure 9: Equivalence between the stress distributions acting in (i) the composite cross-section (with the concrete slab cracked) and (ii) the simplified model (steel I-section restrained by springs).

the elastic bending moment M_z and longitudinal compression N_x must be included as $\overline{W}_2^0$ and $\overline{W}_1^0$ in (12) – they are calculated from the expressions

$$M_z = M_c \cdot \frac{I_{z,a}}{I_{z',c}} \tag{15}$$

$$N_x = M_c \cdot \frac{\overline{y}A_a}{I_{z',c}} \tag{16}$$

where (i) M_c is the moment acting on the composite cross-section, (ii) $I_{z,a}$ is the second moment of area of the steel I-section, about its z axis, (iii) $I_{z',c}$ is the second moment of area of the composite cross-section at the hogging moment region (taking into account the steel I-section and concrete slab rebars), about the z' axis, (iv) A_a is the steel I-section area and (v) $\overline{y}$ is the distance between the neutral axes of the steel I-section and the composite cross-section.

In order to clarify some behavioral features associated with the LDB of I-section steel beams elastically restrained by concrete slabs, constrained-mode GBT buckling analyses of simply supported beams (end cross-sections locally/globally pinned and free to warp) under uniform hogging bending moments were performed. The corresponding results, concerning $E=200GPa$ and $\upsilon=0.3$, are presented and discussed below – the relevant geometrical properties and rotational stiffness values are presented in Table 1. Note that two cross-section dimensions are considered (differing only in the flange thickness – $t_f =12.5, 45$ mm), as well two rotational stiffness values ($k_r =108, 5440$ $kNcm/rad/cm$ – values reported in Calenzani *et al.* (2012) and obtained for typical concrete slabs) – the cross-section dimensions were carefully selected to ensure a high susceptibility to both web single and double curvature lateral-distortional deformations. At this stage, it is worth noting that the effects stemming from non-uniform bending, point of load application (transverse loads are usually applied on top of the concrete slab), shear lag, concrete creep or crack propagation are neglected in this work – considering them requires more realistic models, such as those proposed in Henriques *et al.* (2016, 2020), which include pre-buckling states due to non-uniform bending, visco-elasticity and strain decomposition

Table 1: Rotational stiffness values and geometrical properties of the concrete slabs and restrained steel I-sections.

Model	b_w (mm)	b_f (mm)	t_w (mm)	t_f (mm)	$I_{z,a}$ (cm^4)	A_a (cm^2)	A_s (cm^2/m)	$\overline{y}$ (cm)	$I_{z',c}$ (cm^4)	k_r (kNcm/rad/cm)
B-108-1.25				12.5			4.07	2.279	166809	108 [a]
B-5440-1.25				12.5	152568	138	13.75	8.108	206985	5440 [b]
B-108-4.5	800	300	8	45			4.07	1.016	476890	108 [a]
B-5440-4.5				45	461147	330.4	13.75	3.876	525510	5440 [b]

[a] Fully concrete slab with spacing between beams and slab height equal to 4000 *mm* and 100 *mm*, respectively.
[b] Composite slab with spacing between beams and slab height equal to 2000 *mm* and 200 *mm*, respectively.

procedures. Such features were not considered in this work, since its main purpose is to use constrained GBT deformation modes (i) to shed fresh light on the LDB kinematics and mechanics, and (ii) to obtain reasonably accurate LDB moments with a reduced computational effort.

Through a GBT discretization involving 9 intermediate nodes (2 on each flange and 5 on the web), 17 constrained deformation modes are obtained – Figs. 10 to 13 display the 10 first constrained deformation modes (mode **1** is the axial extension). In particular, it is observed that the constrained deformation modes provide valuable information about the restrained I-section buckling behavior prior to performing any its analysis. For instance, the lack of torsion and lateral-flexural deformations modes implies that LDB is to be expected – this is the case of all the beams analyzed in this section.
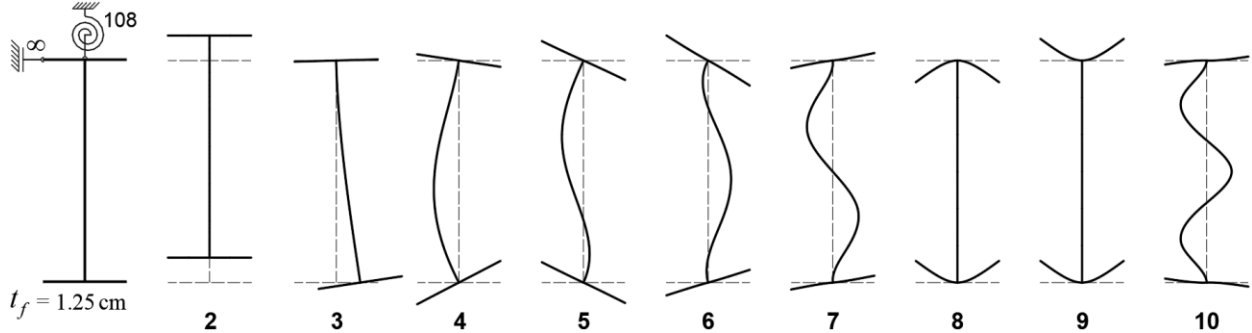
Figure 10: Constrained deformation modes **2**-**10** of the restrained beam B-108-1.25.
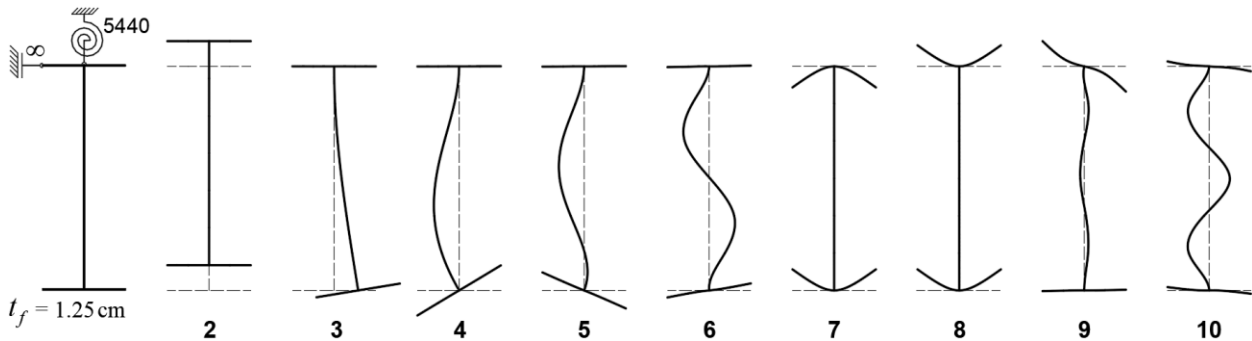
Figure 11: Constrained deformation modes **2**-**10** of the restrained beam B-5440-1.25.

15
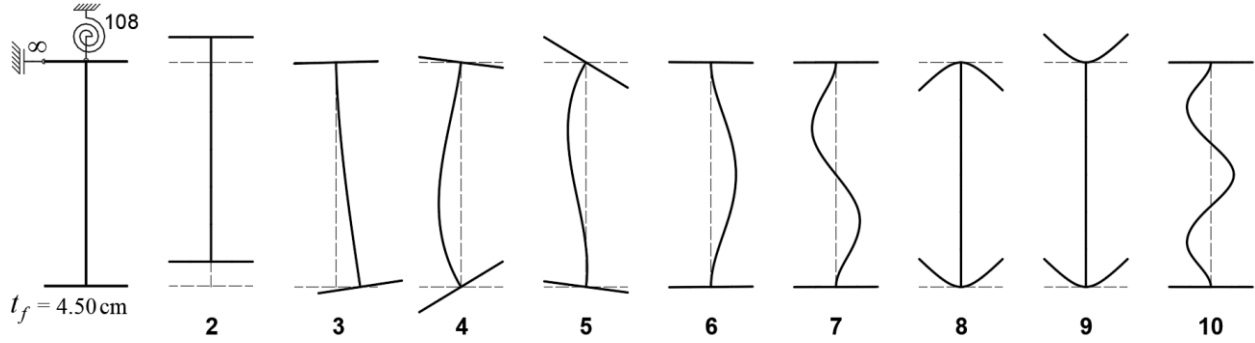
Figure 12: Constrained deformation modes **2**-**10** of the restrained beam B-108-4.5.
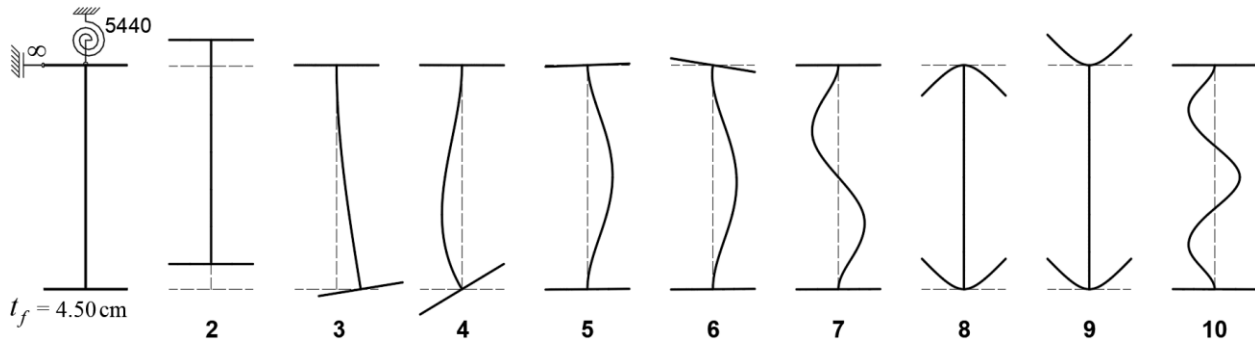
Figure 13: Constrained deformation modes **2**-**10** of the restrained beam B-5440-4.5.

Figs. 14 and 15 make it possible to compare the signature curves M_{cr} vs. L (logarithmic scale) concerning the unrestrained ($k_t = \infty$ and $k_r = 0$) and restrained ($k_t = \infty$ and $k_r = 108$, 5440 $kNcm/rad/cm$) beams with $t_f = 12.5\ mm$ and $t_f = 45\ mm$, respectively. Moreover, the buckled mid-span cross-sections of beam with lengths corresponding to either (i) signature curve local minima or (ii) selected values (when no local minimum exists), as well as the restrained beam modal participation diagrams (based on the constrained deformation modes), are also displayed. In order to validate the proposed approach, based on GBT constrained deformation modes, Figs. 14 and 15 also include M_{cr} values yielded by the programs GBTUL and CUFSM. Concerning these buckling results, it is worth pointing out that:

(i)   Once again, there is an excellent agreement between the critical moments provided by the FSM and two GBT buckling analyses – the maximum difference between the three M_{cr} value sets is 2.6%.

(ii) The signature curves of the beam pairs with $t_f = 12.5\ mm$ (B-108-1.25 and B-5440-1.25) and $t_f = 45\ mm$ (B-108-4.5 and B-5440-4.5) exhibit local minima, associated with web local buckling, at $L=63$ and $60\ cm$, and $L=39$ and $42\ cm$, respectively. The compressed flange rotates in the first beam pair, which does not happen in the second beam pair – all buckling mode shapes involve participations from at least three constrained deformation modes.

(iii) The restrained beam local critical buckling moments are visibly smaller than their unrestrained beam counterparts. The critical buckling moment drop is around 3.8% in beams B-108-1.25 and B-108-4.5, and more pronounced in beams B-5440-1.25 and B-5440-4.5 (around 13.2%) – these drops, which are due to the presence of the rebars under tension (thus increasing the web compressed width), are also reflected in the decrease in the amount web bending appearing in the buckling mode shapes.

16
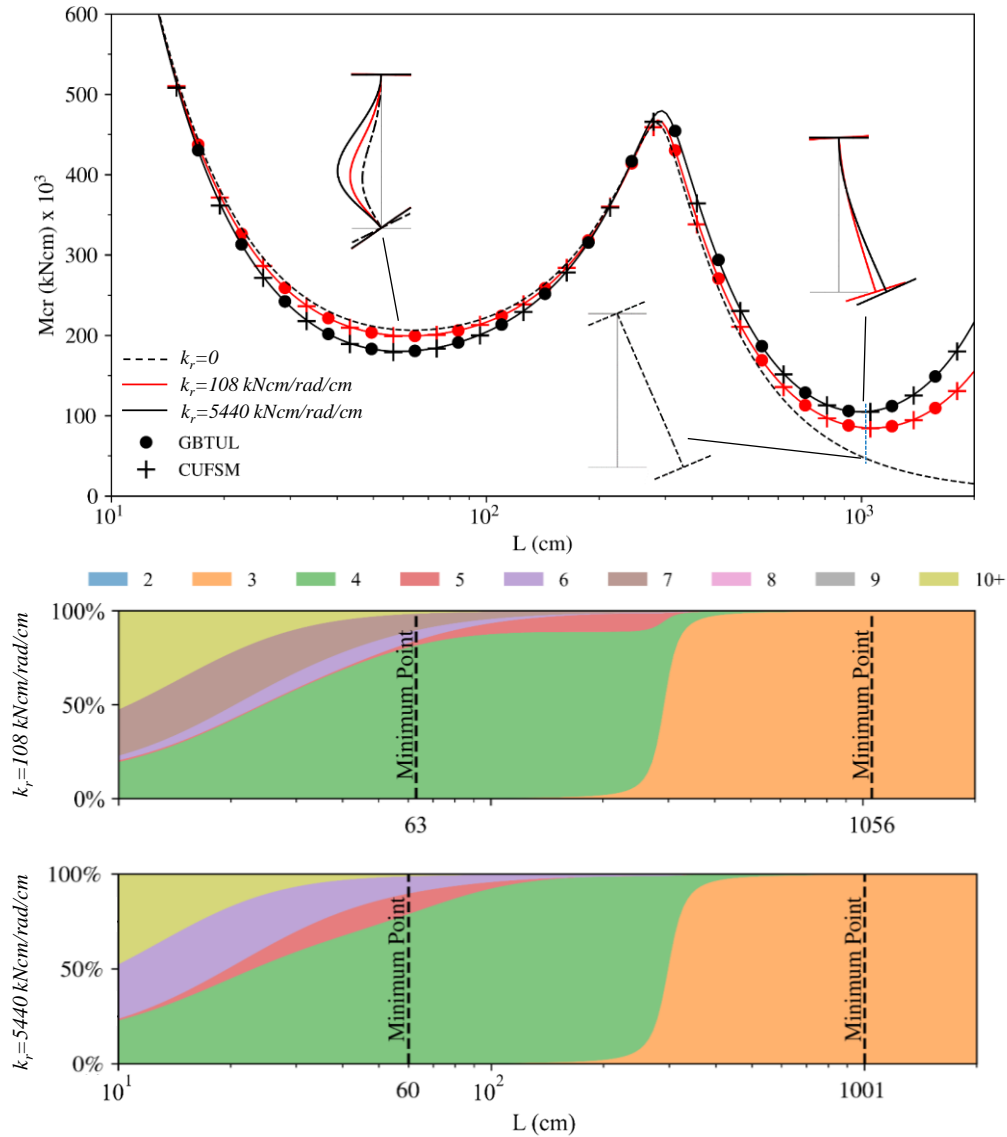
Figure 14: Signature curves M_{cr} vs. L, critical buckling mode shapes and modal participation diagrams (based on constrained deformation modes) of beams B-108-1.25 and B-5440-1.25.

(iv) In the restrained beams, the constraints due to the concrete slab change the buckling mode nature from lateral-torsional to lateral-distortional – the corresponding local minima occur for L=1056 and 1001 cm (beams B-108-1.25 and B-108-4.5 – web single curvature), and for L=1272 and 1206 cm (beams B-5440-1.25 and B-5440-4.5 – web double curvature).

(v) Concrete slabs provide a rotational restraint that is beneficial with respect to LDB. Indeed, the GBT-based (with constrained deformation modes) critical buckling moment increases by 81% (B-108-1.25), 135% (B-5440-1.25), 39% (B-108-4.5) and 50% (B-5440-4.5) – note that the increase is larger when web single curvature is involved.

(vi) By looking at the modal participation diagrams, it can be readily concluded that it is possible to obtain accurate critical LDB moments by including in the GBT buckling analyses either just one (buckling involving web single curvature – mode **3** in beams B-108-1.25 and B-5440-1.25) or two (buckling involving web double curvature – modes **3**+**4** in beams B-108-4.5 and B-108-4.5)

17
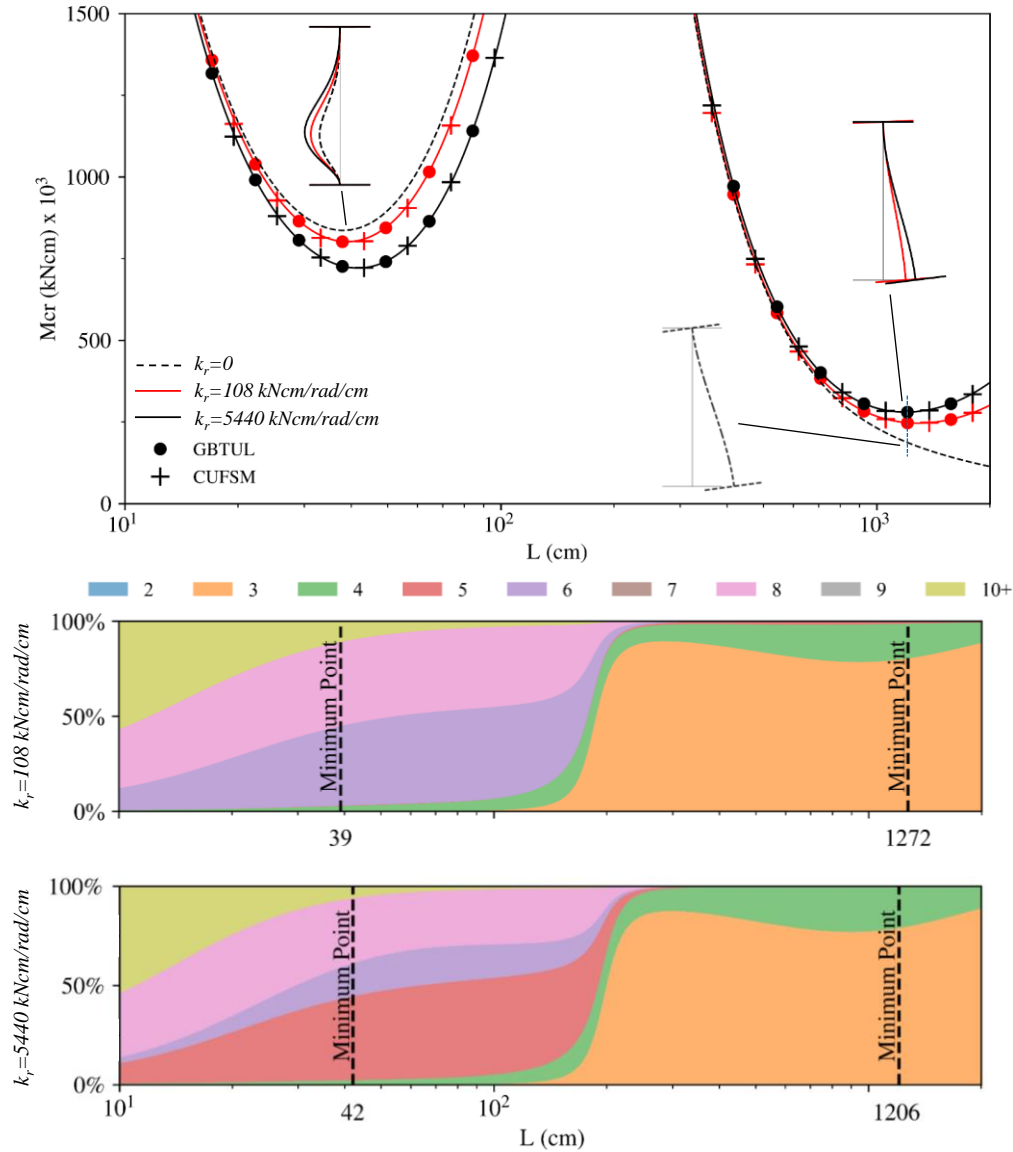
Figure 15: Signature curves M_{cr} vs. L, critical buckling mode shapes and modal participation diagrams (based on constrained deformation modes) of beams B-108-4.5 and B-5440-4.5.

constrained deformation modes. This feature plays a pivotal role in the development of analytical buckling formulae to calculate critical LDB moments, which is addressed in Section 4.

3.2 Lateral-distortional Kinematics

For illustrative purposes, consider the LDB behaviors of beams B-108-1.25 and B-108-4.5, which involve web single (S-LDB) or double (D-LDB) curvature, respectively. Figs. 16 and 17 show how the modal participations make it possible to quantify the contribution of each GBT cross-section deformation mode to the beam LDB modes. This GBT feature is crucial to enable an accurate determination of the lateral-distortional deformations, as well as to acquire an in-depth understand of the associated kinematics. It is worth noting that:
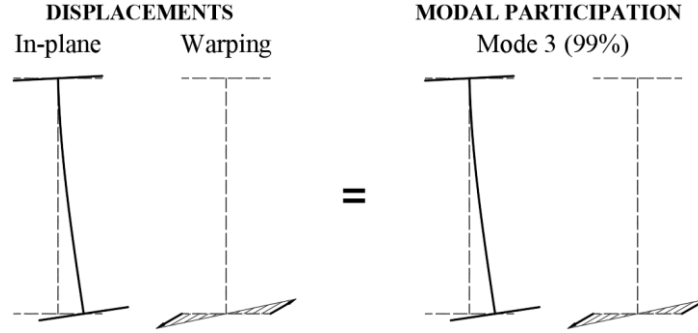
Figure 16: Beam B-108-1.25: in-plane and warping displacements, and GBT modal decomposition of the S-LDB.
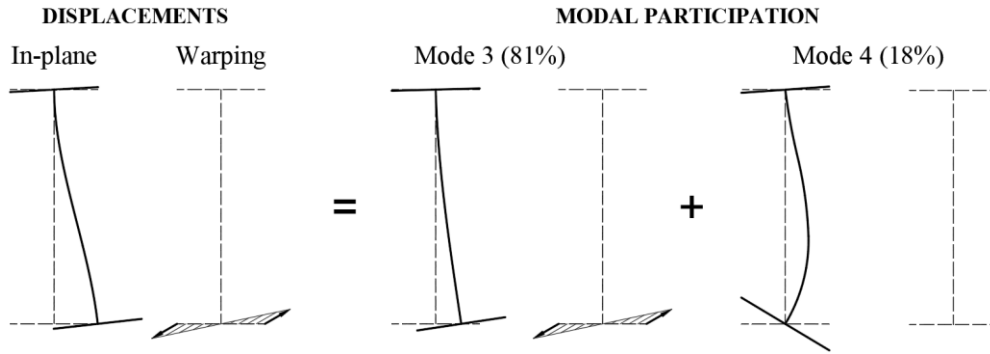
Figure 17: Beam B-108-4.5: in-plane and warping displacements, and GBT modal decomposition of the D-LDB.

(i) The single curvature lateral-distortional deformation is characterised by the simultaneous occurrence of (i_1) a rigid-body rotation of the bottom flange about the top web-flange junction, due to a non-negligible linear variation of the warping displacements, and (i_2) the transverse bending of the web, due to the wall kinematic compatibility at the web-flange junctions. These transverse and warping displacements are captured almost exclusively by the GBT constrained deformation mode **3**.

(ii) The web double curvature lateral-distortional deformation combines two GBT constrained deformation modes, namely a dominant lateral-distortional mode **3** and a constrained local mode **4** – the latter involves (ii_1) web transverse bending, (ii_2) no in-plane displacements of the web-flange junctions (natural internal nodes) and (ii_3) null warping displacements.

(iii) By looking at the constrained deformation modes **3** and **4**, it is possible to clearly identify the key degrees of freedom governing the lateral-distortional deformation − (iii_1) the lateral displacement of the (unconnected) bottom flange and (iii_2) the flange rotations.

As done by Silvestre & Camotim (2010), in the context of unrestrained lipped channel cross-sections and to enable a better understanding of the distortion mechanics, a set of kinematical assumptions is also adopted in this work. They simplify both (i) the procedure to determine lateral-distortional displacements in restrained I-sections and (ii) the final solution, with little impact on its accuracy. Such kinematical assumptions are:

(i) Null transverse extension (ε_{ss}=0) in each cross-section wall, which implies $\partial v / \partial s = 0$. Then, it becomes possible to conclude that the transverse v-displacement must be uniform within each wall, *i.e.*, and does not vary with the mid-line coordinate s.

19

(ii) Null shear strain ($\gamma_{xs}=0$) in each cross-section wall mid-plane, which implies $\partial u / \partial s = -\partial v / \partial x$. This assumption leads, straightforwardly, to

$$u = -\int v \, ds \qquad . \quad (17)$$

(iii) The walls exhibiting significant warping displacements $u(s)$ do not bend transversely, *i.e.*, undergo only rigid-body motions – their transverse bending curvatures are null ($\partial^2 w / \partial s^2 = 0$).

(iv) The total warping is primary (secondary warping is neglected) and deemed uniform along the wall thickness (z direction).

The above first two assumptions mentioned concern the wall membrane behaviour and are widely adopted in the context of FSM (*e.g.*, Li & Schafer 2010) and GBT (*e.g.*, Schardt 1989, Silvestre & Camotim 2002 and Dinis *et al.* 2006) analyses. Moreover, since (i) the lateral/flexural and torsional stiffness values provided by the concrete slab are visibly larger than those provided by the (connected) top flange, and (ii) the shear connection deformation is neglected, it can be assumed that transverse bending does not occur on the top flange – it rigidly "follows" the slab rotation (*e.g.*, Zhou *et al.* 2016 and Bradford 1998).

In order to obtain simplified (but accurate) expressions to determine the lateral-distortional displacement field, it is necessary to separate the key degrees of freedom (DOFs) characterising the GBT constrained deformation modes **3** (lateral-distortional) and **4** (local), through the imposition of unit displacements and/or rotations. This is done by first looking at the simplest possible GBT cross-section analysis, which involves the six natural nodes (two internal and four end) and a total of 24 DOFs (4 per node – see Fig. 18(a)) and realising that this number is clearly excessive for a simplified model. However, on the basis of the (i) adopted kinematical assumptions (described above) and (ii) observation of the GBT constrained deformation mode shapes displayed in Figs. 16 and 17, it is possible to obtain a simplified characterisation of the displacement fields involved without performing a GBT cross-section analysis. It requires imposing localised displacement restraints on a plane frame finite element model formed by the three cross-section walls, with local coordinate axes x^i, s^i, z^i and displacement components u^i, v^i, w^i, as described next:

(a)　　　　　　　　　(b)　　　　　　　　　(c)
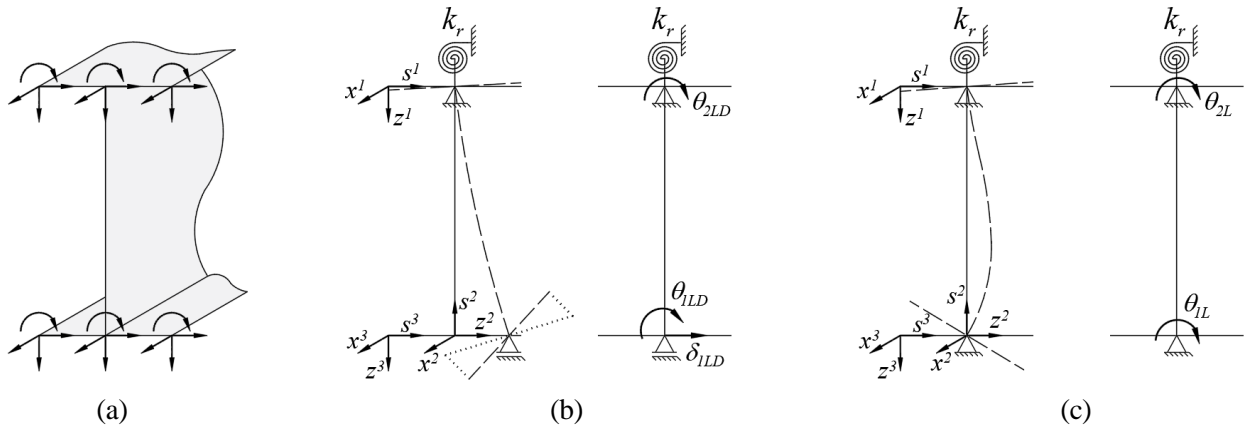
Figure 18: (a) Degrees of freedom assigned to each node in a GBT discretization and cross-section plane frame models used to characterize the (b) lateral-distortional and (c) local deformations.

20

(i) Characterize the lateral-distortional deformation through three nodal DOFs: (i_1) lateral displacement of the (unconstrained) bottom flange (δ_{1LD}), (i_2) rotation of the bottom flange-web junction (θ_{1LD}) and (i_3) rotation at the top flange-web junction (θ_{2LD}) – in addition, as shown in Fig. 18(b), three in-plane transverse displacements are fully restrained.

(ii) Characterize the local deformation through two nodal DOFs: (ii_1) rotation of the bottom flange-web junction (θ_{1L}) and (ii_2) rotation of the top flange-web junction (θ_{2L}) – in addition, as shown in Fig. 18(c), four in-plane transverse displacements are fully restrained.

On the basis of the previous remarks, the following procedure can be adopted to determine the key DOFs defining the lateral-distortional and local displacement fields:

(i) Using one 2-node element with two DOFs per node and adopting Hermite cubic polynomials to approximate the web flexural displacement function (see Fig. 19), determine the web elementary stiffness matrix $[K^w]$, given by

$$[K^w] = \begin{bmatrix} \dfrac{12D_w}{b_w^3} & \dfrac{6D_w}{b_w^2} & \dfrac{-12D_w}{b_w^3} & \dfrac{6D_w}{b_w^2} \\[2mm] & \dfrac{4D_w}{b_w} & \dfrac{-6D_w}{b_w^2} & \dfrac{2D_w}{b_w} \\[2mm] & & \dfrac{12D_w}{b_w^3} & \dfrac{-6D_w}{b_w^2} \\[2mm] sym. & & & \dfrac{4D_w}{b_w}+k_r \end{bmatrix} \tag{18}$$

with

$$D_w = \frac{Et_w^3}{12(1-\upsilon^2)} \qquad . \tag{19}$$

(ii) Assemble the system of linear equilibrium equations (cast in matrix form) partitioned with respect to the sets of specified and unspecified displacements and/or rotations (*e.g.*, Reddy 2006), *i.e.*,

Figure 19: Degrees of freedom associated with flexural displacement function of the web approximated through Hermite cubic polynomials

21

$$\{U\} = [K_{uu}]^{-1}(\{F\} - [K_{ur}]\{d\}) \qquad , \quad (20)$$

where (ii$_1$) $\{d\}$ is the displacement vector of specified (known) variables, (ii$_2$) $\{U\}$ is the displacement vector of unspecified (unknown) variables, (ii$_3$) $\{F\}$ is the vector of applied forces, (ii$_4$) $[K_{uu}]$ is the (symmetric) condensed stiffness matrix and (ii$_5$) $[K_{ur}]$ is a matrix containing cross-stiffness terms associated with the specified displacements/rotations.

(iii) For lateral-distortional deformation: by imposing the boundary conditions shown in Fig. 18(b), with displacement $\delta_{1LD} = 1$, in system (20), the rotations θ_{1LD} and θ_{2LD} are obtained as

$$\begin{Bmatrix} \theta_{1LD} \\ \theta_{2LD} \end{Bmatrix} = \begin{bmatrix} K_{22}^w & K_{24}^w \\ K_{42}^w & K_{44}^w \end{bmatrix}^{-1} \cdot \left(\begin{Bmatrix} F_2 \\ F_4 \end{Bmatrix} - \begin{bmatrix} K_{21}^w & K_{23}^w \\ K_{41}^w & K_{43}^w \end{bmatrix} \cdot \begin{Bmatrix} d_1 \\ d_3 \end{Bmatrix} \right) = \begin{Bmatrix} \dfrac{-3(2D_w + b_w k_r)}{2b_w(3D_w + b_w k_r)} \\ \dfrac{-3D_w}{b_w(3D_w + b_w k_r)} \end{Bmatrix} \qquad , \quad (21)$$

where $F_2 = F_4 = 0$, $d_1 = \delta_{1LD} = 1$ and $d_3 = 0$.

(iv) For local deformation: by imposing the boundary conditions shown in Fig. 18(c), with displacement $\theta_{1L} = 1$, in system (20), the rotation θ_{2L} is obtained as

$$\{\theta_{2L}\} = \left[K_{44}^w \right]^{-1} \cdot \left(\{F_4\} - \begin{bmatrix} K_{41}^w & K_{42}^w & K_{43}^w \end{bmatrix} \cdot \begin{Bmatrix} d_1 \\ d_2 \\ d_3 \end{Bmatrix} \right) = \left\{ \dfrac{-2D_w}{4D_w + b_w k_r} \right\} \qquad , \quad (22)$$

where $F_4 = 0$, $d_1 = d_3 = 0$ and $d_2 = \theta_{1L} = 1$.

After defining the key DOF values, the next step is to derive the displacement and rotation functions along the cross-section mid-line. Since the I-section is doubly symmetric, it is easily concluded that, in the lateral-distortional deformation, the bottom flange warping displacement profile $u_{LD}^3(s)$ is anti-symmetric and varies linearly with the mid-line coordinate s – thus, the membrane transverse displacement (v_{LD}^3) is constant in this wall. On the other hand, the transverse flexural displacements $w(s)$ can be approximated by means of (i) linear functions $w_k^1(s)$ and $w_k^3(s)$, respectively for the top (connected) and bottom (unconnected) flanges (recall the rigid-body motion assumption), and (ii) an Hermite cubic polynomial $w_k^2(s)$, for the web. Then, the displacement profiles are given by ($0 \le s \le b_w$, for the web, and $0 \le s \le b_f$, for the flanges)

(i) For lateral-distortional deformation (with $\delta_{1LD} = 1$):

$$u_{LD}^1 = u_{LD}^2 = 0$$
$$u_{LD}^3(s) = \frac{b_f}{2}\left(1 - 2\frac{s}{b_f}\right) \qquad\qquad\qquad (23)$$

$$v_{LD}^1 = v_{LD}^2 = 0$$
$$v_{LD}^3 = 1 \qquad\qquad\qquad (24)$$

$$w_{LD}^1(s) = -\frac{b_f \theta_{2LD}}{2}\left(1 - 2\frac{s}{b_f}\right)$$

$$w_{LD}^2(s) = s\theta_{1LD} + \frac{s^2(-3 - 2b_w\theta_{1LD} - b_w\theta_{2LD})}{b_w^2} + \frac{s^3(2 + b_w\theta_{1LD} + b_w\theta_{2LD})}{b_w^3} \qquad . \quad (25)$$

$$w_{LD}^3(s) = -\frac{b_f \theta_{1LD}}{2}\left(1 - 2\frac{s}{b_f}\right)$$

Note that, when $k_r \to 0$ in (25), the lateral-torsional (**LT**) deformation, associated with a centre of rotation located at the top flange-web junction, is characterised by

$$u_{LT}^1 = u_{LT}^2 = 0$$
$$u_{LT}^3(s) = \frac{b_f}{2}\left(1 - 2\frac{s}{b_f}\right) \qquad (26)$$

$$v_{LT}^1 = v_{LT}^2 = 0$$
$$v_{LT}^3 = 1 \qquad (27)$$

$$w_{LT}^1(s) = w_{LT}^3(s) = \frac{b_f}{2b_w}\left(1 - 2\frac{s}{b_f}\right) \qquad (28)$$
$$w_{LT}^2(s) = 1 - \frac{s}{b_w}$$

$$w_{LT,s}^1 = w_{LT,s}^2 = w_{LT,s}^3 = -\frac{1}{b_w} \qquad . \quad (29)$$

(ii) For local deformation (with $\theta_{1L} = 1$):

$$u_L^1 = u_L^2 = u_L^3 = 0 \qquad (30)$$

$$v_L^1 = v_L^2 = v_L^3 = 0 \qquad (31)$$

$$w_L^1(s) = -\frac{b_f \theta_{2L}}{2}\left(1 - 2\frac{s}{b_f}\right)$$

$$w_L^2(s) = s - \frac{s^2(2 + \theta_{2L})}{b_w} + \frac{s^3(1 + \theta_{2L})}{b_w^2} \qquad . \quad (32)$$

$$w_L^3(s) = -\frac{b_f}{2}\left(1 - 2\frac{s}{b_f}\right)$$

4. Analytical Formulae

Denoting (i) the bifurcation stress parameter of the restrained steel I-section beam bifurcation by λ_b and (ii) the corresponding compressive load and bending moment reference values by N_x and M_z, bifurcation

occurs when the applied stress resultants reach the values $N_{a,b} = \lambda_b N_x$ and $M_{a,b} = \lambda_b M_z$. Note that, if a unit M_c value is imposed in Eqs. (15) and (16), λ_b provides the bifurcation moment acting on the composite cross-section ($M_{c,b}$). Then, the GBT equation subsystem concerning the lateral-distortional (**LD**) and local (**L**) deformation modes, defined in Section 3, reads

$$[C]\begin{Bmatrix}\varphi_{LD,xxxx}\\\varphi_{L,xxxx}\end{Bmatrix} + \left([D]-[E]^{\mathrm{T}}-[E]\right)\begin{Bmatrix}\varphi_{LD,xx}\\\varphi_{L,xx}\end{Bmatrix} + [B]\begin{Bmatrix}\varphi_{LD}\\\varphi_{L}\end{Bmatrix} + \lambda_b\left(N_x[X_1]+M_z[X_2]\right)\begin{Bmatrix}\varphi_{LD,xx}\\\varphi_{L,xx}\end{Bmatrix} = 0 \quad , \quad (33)$$

where (i) $[X_1]$ and $[X_2]$ are geometric stiffness matrices, (ii) $[C]$, $[D]$, $[E]$ and $[B]$ are linear stiffness matrices and (iii) N_x and M_z are positive for axial compression and hogging bending moments. Adopting the geometrical parameters

$$\alpha = \frac{b_f}{b_w} \qquad\qquad \beta = \frac{t_f}{t_w} \qquad , \quad (34)$$

the determination of cross-section modal mechanical properties and cross-section geometric stiffness components leads to

(i) Matrix $[C]$ – related to warping displacements:

$$[C] = \frac{b_w^3}{420}\begin{bmatrix} C_{LD} & 0 \\ 0 & C_L \end{bmatrix} \qquad , \quad (35)$$

where, as mentioned above,

$$\begin{aligned} C_{LD} &= C_{11} = 35Et_w\alpha^3\beta \\ C_L &= C_{22} = D_w[35\alpha^3\beta^3(1+\theta_{2L}^2)+2(2-3\theta_{2L}+2\theta_{2L}^2)] \end{aligned} \qquad , \quad (36)$$

the secondary warping involved in lateral-distortional deformation is neglected (flexural term in Eq. (5)) and it is recalled that local deformation involves no primary warping (membrane term in Eq. (5)).

(ii) Matrix $[D]$ – related to torsional deformation:

$$[D] = \frac{Gt_w^3}{90b_w}\begin{bmatrix} D_{LD} & D_{LD\text{-}L} \\ sym. & D_L \end{bmatrix} \qquad , \quad (37)$$

where

$$\begin{aligned} D_{LD} &= D_{11} = 36+6b_w(\theta_{1LD}+\theta_{2LD})+b_w^2[(4+30\alpha\beta^3)\theta_{1LD}^2-2\theta_{1LD}\theta_{2LD}+2(2+15\alpha\beta^3)\theta_{2LD}^2] \\ D_{LD\text{-}L} &= D_{12} = b_w\left\langle 3+b_w[(4+30\alpha\beta^3)\theta_{1LD}-\theta_{2LD}]+\theta_{2L}\{3+b_w[-\theta_{1LD}+2(2+15\alpha\beta^3)\theta_{2LD}]\}\right\rangle \quad (38) \\ D_L &= D_{22} = 2b_w^2[2+15\alpha\beta^3-\theta_{2L}+(2+15\alpha\beta^3)\theta_{2L}^2] \end{aligned}$$

and it should be noted that the membrane shear distortion is deemed null (first term in Eq. (7)).

(iii) Matrix $[E]$ – related to flexural Poisson effects:

$$[E] = \frac{\upsilon b_w D_w}{15}\begin{bmatrix} 0 & 0 \\ 0 & E_L \end{bmatrix} \qquad , \quad (39)$$

where

$$E_L = E_{22} = -2 + \theta_{2L} - 2\theta_{2L}^2 \qquad , \quad (40)$$

and it is readily observed that Vlasov's null transverse extension assumption is adopted (*i.e.*, the membrane term in Eq. (8) is null) and the transverse bending Poisson effects involved in the lateral-distortional deformation are neglected (flexural term in Eq. (8)), as admitted in Silvestre (2010).

(iv) Matrix [B] – related to transverse bending of the walls and to the elastic spring stiffness:

$$[\text{B}] = \begin{bmatrix} B_{LD} & 0 \\ 0 & B_L \end{bmatrix} \qquad , \quad (41)$$

where

$$B_{LD} = B_{11} = k_r \theta_{2LD}^2 + \frac{4D_w}{b_w^3}[3 + b_w^2(\theta_{1LD}^2 + \theta_{1LD}\theta_{2LD} + \theta_{2LD}^2) + 3b_w(\theta_{1LD} + \theta_{2LD})]$$

$$\qquad , \quad (42)$$

$$B_L = B_{22} = k_r \theta_{2L}^2 + \frac{4D_w}{b_w}(1 + \theta_{2L} + \theta_{2L}^2)$$

and it should be noted, once again, that the null transverse extension assumption is adopted.

(v) Matrix $[\text{X}_1]$ – associated with the pre-buckling uniform longitudinal stresses:

$$[\text{X}_1] = \frac{b_w t_w}{420 A_a} \begin{bmatrix} X_{1.LD} & X_{1.LD-L} \\ sym. & X_{1.L} \end{bmatrix} \qquad , \quad (43)$$

where

$$X_{1.LD} = X_{1.11} = 156 + 420\alpha\beta + b_w(44\theta_{1LD} - 26\theta_{2LD}) + b_w^2[(4 + 35\alpha^3\beta)\theta_{1LD}^2 -$$
$$- 6\theta_{1LD}\theta_{2LD} + (4 + 35\alpha^3\beta)\theta_{2LD}^2]$$
$$X_{1.LD-L} = X_{1.12} = b_w\{22 + b_w[(4 + 35\alpha^3\beta)\theta_{1LD} - 3\theta_{2LD}]\} + \theta_{2L}b_w\{-13 + \qquad . \quad (44)$$
$$+ b_w[-3\theta_{1LD} + (4 + 35\alpha^3\beta)\theta_{2LD}]\}$$
$$X_{1.L} = X_{1.22} = b_w^2[4 + 35\alpha^3\beta - 6\theta_{2L} + (4 + 35\alpha^3\beta)\theta_{2L}^2]$$

(vi) Matrix $[\text{X}_2]$ – associated with the pre-buckling bending stresses:

$$[\text{X}_2] = \frac{b_w^2 t_w}{840 I_{z.a}} \begin{bmatrix} X_{2.LD} & X_{2.LD-L} \\ sym. & X_{2.L} \end{bmatrix} \qquad , \quad (45)$$

where

$$X_{2.LD} = X_{2.11} = 84(1 + 5\alpha\beta) + 2b_w(8\theta_{1LD} - \theta_{2LD}) + b_w^2(1 + 35\alpha^3\beta)(\theta_{1LD}^2 - \theta_{2LD}^2)$$
$$X_{2.LD-L} = X_{2.12} = b_w\{8 + (1 + 35\alpha^3\beta)b_w\theta_{1LD} - \theta_{2L}[1 + (1 + 35\alpha^3\beta)b_w\theta_{2LD}]\} \qquad . \quad (46)$$
$$X_{2.L} = X_{2.22} = -b_w^2[(1 + 35\alpha^3\beta)(\theta_{2L}^2 - 1)]$$

Once functions $\varphi_{LD}(x)$ and $\varphi_L(x)$ are known, it is possible to obtain the formulae providing bifurcation stress estimates – such functions can be cast in the form

$$\varphi_{LD} = d_{LD}\phi(x) \qquad\qquad \varphi_L = d_L\phi(x) \qquad\qquad , \quad (47)$$

where (i) d_{LD} and d_L are deformation mode amplitudes and (ii) $\phi(x)$ is a unit shape function describing (exactly or approximately) their longitudinal variation. Introducing Eq. (47) in Eq. (33) and applying Galerkin's method, with sinusoidal approximation functions, one is led to an eigenvalue problem for simply supported beams (end cross-sections locally/globally pinned and free to warp), expressed as

$$\left(\begin{bmatrix} K_{11} & K_{12} \\ K_{21} & K_{22} \end{bmatrix} - \lambda_b \begin{bmatrix} G_{11} & G_{12} \\ G_{21} & G_{22} \end{bmatrix} \right) \cdot \begin{Bmatrix} d_{LD} \\ d_L \end{Bmatrix} = 0 \qquad\qquad , \quad (48)$$

with

$$K_{ik} = C_{ik}\left(\frac{\eta\pi}{L}\right)^2 + \left(D_{ik} - E_{ki} - E_{ik}\right) + B_{ik}\left(\frac{\eta\pi}{L}\right)^{-2} \qquad\qquad (49)$$

$$G_{ik} = N_x X_{1.ik} + M_z X_{2.ik} \qquad\qquad , \quad (50)$$

where η is the number of longitudinal half-waves exhibited by deformation mode.

Solving analytically the eigenvalue problem defined by Eq. (48) leads to the web single/double curvature lateral-distortional bifurcation moment $M_{c.b}$ (*i.e.*, the lowest positive value of λ_b if a unit pre-bifurcation value M_c is imposed), for a given L,

$$\lambda_b = M_{c.b} = \frac{-b \pm \sqrt{b^2 - 4ac}}{2a} \qquad\qquad , \quad (51)$$

where

$$\begin{aligned} a &= G_{11}G_{22} - G_{12}G_{21} \\ b &= -G_{22}K_{11} - G_{11}K_{22} + G_{12}K_{12} + G_{21}K_{21} \\ c &= K_{11}K_{22} - K_{12}K_{21} \end{aligned} \qquad . \quad (52)$$

When lateral-distortional bifurcation involves exclusively <u>web single curvature</u> ($M_{c.b} \equiv M_{c.b}^S$) the dimension of the eigenvalue problem (Eq. (48) is reduced to 1 and, therefore, the estimate of $M_{c.b}^S$ is given by

$$M_{c.b}^S = \frac{1}{N_x X_{1.LD} + M_z X_{2.LD}} \left[C_{LD}\left(\frac{\eta\pi}{L}\right)^2 + D_{LD} + B_{LD}\left(\frac{\eta\pi}{L}\right)^{-2} \right] \qquad . \quad (53)$$

Moreover, the critical length L_{cr}^S, associated with the minimum single curvature lateral-distortional bifurcation moment $M_{c.b.min}^S$, is readily obtained by finding the relevant root of $dM_{c.b}^S / dL = 0$, which is provided by the formula (for $\eta = 1$)

$$L_{cr}^S = \pi \sqrt[4]{\frac{C_{LD}}{B_{LD}}} \tag{54}$$

and corresponds to

$$M_{c.b.\min}^S = \frac{2\sqrt{C_{LD}B_{LD}} + D_{LD}}{N_x X_{1.LD} + M_z X_{2.LD}} \,. \tag{55}$$

On the other hand, the critical length (L_{cr}) corresponding to a minimum λ_b ($\lambda_{b.\min.}$ or $M_{c.b.\min}$, for a unit M_c value) associated with either **LD** + **L** deformations (*i.e.*, web double curvature – L_{cr}^D) or dominant (but not exclusive) **LD** deformations (*i.e.*, web single curvature – L_{cr}^S), is also the relevant root of $d\lambda_b / dL = 0$. However, because Eq. (48) has dimension 2, function $\lambda_b(L)$ is highly non-linear (see Eq. (51)) and the exact value of this root cannot be determined analytically. In order to overcome this difficulty, an approximate and somewhat empirical procedure was adopted, in which the determination of the single or double curvature LDB moment must be preceded by an estimate of the longitudinal half-wave number (η) associated with the beam length L. This procedure is based on (i) the observation, for a rather large number of cases, that the difference between L_{cr}^D and L_{cr}^S rarely exceeds 15%, and (ii) the fact that L_{cr}^S can be calculated/estimated analytically (using Eq. (54)). Its first step consists of finding the two positive integer numbers adjacent to the ratio L / L_{cr}^S – they are denoted η_1 and η_2. Then, insert η_1 and η_2 in Eq. (49) and solve the two ensuing eigenvalue problems to obtain the corresponding bifurcation parameters $\lambda_{b.1}$ and $\lambda_{b.2}$, respectively. Finally, use the lowest value between $\lambda_{b.1}$ and $\lambda_{b.2}$ to estimate the lateral-distortional buckling moment.

The eigenvector associated with λ_b provides the participations of the **LD** and **L** deformation modes in the beam buckling mode, given by the strain energy percentages associated with each of the two modes, *i.e.*,

$$MP_{LD}(\%) = \frac{K_{11}(K_{12} - \lambda_b G_{12})^2}{K_{11}(K_{12} - \lambda_b G_{12})^2 + K_{22}(K_{11} - \lambda_b G_{11})} \times 100 \qquad MP_L(\%) = 100 - MP_{LD}(\%) \,. \tag{56}$$

It is still worth noting that the GBT-based formulae incorporate genuine folded-plate theory, a feature that (i) ensures their accuracy and universality and (ii) makes it possible to overcome the limitations exhibited by the lateral-distortional buckling formulae currently available in the literature. While some of them are based on the assumption of fully fixed (connected) top flanges (*e.g.*, Silvestre 2010 and Zhou *et al.* 2016), others do not cover the web double curvature case (*e.g.*, Hansville *et al.* 1998 and Dias *et al.* 2019). Moreover, the decomposition of the GBT-based buckling solution into constrained lateral-distortional and local deformation modes provides in-depth insight into the mechanics involved. The elegance and usefulness of the approach proposed in this work stems from the fact that a single easy-to-use analytical formula enables researchers and engineers to obtain lateral-torsional (for $k_r = 0$) and lateral-distortional (involving web single or double curvature) buckling moments of elastically restrained I-section beams, namely those appearing in composite steel-concrete beams.

4.1 Illustration, Validation and Accuracy
In order to illustrate the application, validate and assess the accuracy of the derived constrained-mode GBT-based formulae to estimate beam lateral-distortional buckling moments, they are applied next

to the restrained beams described in Table 1 and also an unrestrained beam with t_f=12.5 mm (k_t=∞ and $k_r = 0$ – B-0-1.25), all with several lengths. Fig. 20 shows the variations of the buckling moment M_{cr} with the length L (logarithmic scale) provided by the analytical formulae (solid curves – with $\eta \geq 1$ in Eq. (51)) – the buckling mode half-wave numbers are given inside brackets. Besides the values yielded by the analytical formulae, Fig. 20 also includes, for validation and comparison purposes, solid circles corresponding to critical buckling moments obtained from GBT-based analyses ($\eta \geq 1$) including all (non-constrained) deformation modes and performed in the GBTUL program. As for Fig. 21, it displays some beam buckled mid-span cross-sections (shapes and modal participations), together with their respective buckling moments, which (i) correspond to either critical lengths (local minima of the signature curves) or selected beam lengths (when no such minima exist), and (ii) are obtained by means of either the analytical formulae or conventional GBT buckling analyses. The observation of this set of results prompts the following remarks:

(i)   The critical buckling moment estimates are provided by the lower portions of the various individual bifurcation curves (associated with η =1, η =2, …), located between their intersection points.

(ii)   The GBT-based formulae yield accurate (ii₁) lateral-torsional and lateral-distortional (involving web single or double curvature) buckling moments, and (ii₂) associated critical lengths – the errors never exceed 1.0%.

(iii)   There is also very close agreement between the buckling mode shapes provided by the analytical procedure and those obtained through conventional GBT analyses.

(iv)   By looking at the modal participations, it is possible to obtain meaningful information about the lateral-distortional mechanics – indeed, it is possible to conclude that web double curvature plays a more relevant role in the buckling behaviour beam B-5440-4.5, since its buckling mode shape exhibits a larger contribution from local deformation (MP$_L$ = 21.2%).
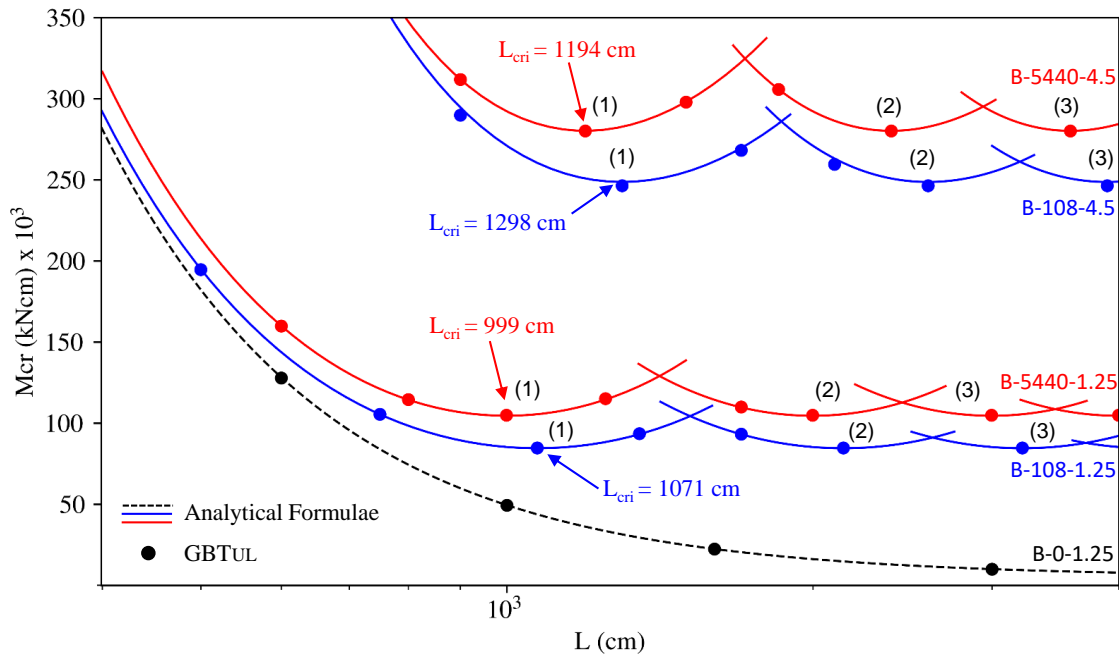
Figure 20: Lateral-distortional buckling moment signature curves yielded by the analytical formulae and GBT analyses.

	B-0-1.25	B-108-1.25	B-5440-1.25	B-108-4.5	B-5440-4.5	
	1000.00 cm	1070.96 cm	999.39 cm	1297.83 cm	1193.74 cm	Lcr (mm)
	49.446×10^3	84.503×10^3	104.523×10^3	248.631×10^3	280.155×10^3	Mcr (kNcm)
Analytical Formulae						Buckling Mode Shape
	$MP_{LD} \equiv MP_{LT} = 100\%$	$MP_{LD} = 99.8\%$ $MP_L = 0.2\%$	$MP_{LD} = 99.7\%$ $MP_L = 0.3\%$	$MP_{LD} = 81.1\%$ $MP_L = 18.9\%$	$MP_{LD} = 78.8\%$ $MP_L = 21.2\%$	Modal Participation
	1000.00 cm	1069.17 cm	996.49 cm	1297.09 cm	1193.93 cm	Lcr (mm)
	49.381×10^3	84.686×10^3	104.896×10^3	246.332×10^3	280.106×10^3	Mcr (kNcm)
GBTUL						Buckling Mode Shape

Figure 21: Critically buckled mid-span cross-sections based on analytical formulae and GBTUL deformation modes.

Finally, an assessment of the LDB behavior of simply supported I-section steel beams with dimensions $b_w = 600\,mm$, $b_f = 200\,mm$, $t_w = 12.5\,mm$ and $t_f = 16, 25, 45, 50\,mm$, and length $L = 700\,cm$, is presented next[8]. The steel beams are acted by uniform negative (hogging) bending moments and restrained by concrete slabs with (i) height 200 mm and (ii) top and bottom steel rebar areas of 11.25 cm^2/m or 7.20 cm^2/m – note that the influence of the steel rebars on the LDB behavior is also assessed. Moreover, three realistic rotational stiffness values are adopted, namely $k_r = 250, 500, 2500$ $kNcm/rad/cm$. Table 2 shows the beam critical moment estimates, together with the respective longitudinal half-wave numbers and the modal participations of the associated LDB mode (**LD** and **L** deformation modes), provided by the GBT-based analytical formulae. The B-*-* beam models take into account the presence of the steel rebars, which are neglected by their B0-*-* counterparts. Table 2 also includes critical moment estimates provided by the formulae due to Silvestre (2010), Hanswille *et al.* (1998), Zhou *et al.* (2017) and Dias *et al.* (2019)[9]. For validation purposes, the buckling moment estimates obtained in this work are

---

also compared with values yielded by ANSYS (SAS 2013) SFEA[10]. Fig. 22 displays several critical buckling mode shapes obtained from either the proposed analytical formulae or the ANSYS SFEA. A close observation of this set of results prompts the following remarks:

(i) There is an excellent agreement between the critical moments provided by the proposed analytical formulae and shell buckling analyses. Indeed, the average difference between the two sets of M_{cr} values is 1.8% (standard deviation of 0.012), with a maximum of 4.9% occurring for beam B0-250-5.0 –the small discrepancies probably arise from the thin-walled plate assumptions considered, leading to slightly different warping distributions in thick flanges, such as those exhibited by some of the beams analysed (t_f = 45 and 50 *mm*).

(ii) The buckling mode shapes obtained from the proposed analytical formulae and ANSYS analyses, shown in Fig. 22, are remarkably similar. Moreover, the modal participations yielded by GBT-based formulae provide insight on the web curvature behaviour – indeed, the LDB mode shapes with web single and double curvature exhibit very different **L** deformation mode contributions – about 1% in S-LDB and 13% in D-LDB.

(iii) While the LDB mode shapes of the beams with t_f = 16 and 25 *mm* (t_f/t_w = 1.28 and 2) exhibit web single curvature, those of beams with t_f = 45 and 50 *mm* (t_f/t_w = 3.6 and 4) have web double curvature.

(iv) The additional strength stemming from the presence of the steel rebars, and ensuing compressive stress reduction in the bottom flange, leads to an LDB moment increase value ranging from 5.7% (beam B-250-5.0) to 14.1% (beam B-2500-1.6).

(v) As expected, the largest differences between the results provided by the SFEA and Silvestre's model (Silvestre 2010), varying between 24% and 60%, are due to the fact that this model assumes a fully restrained top flange (*i.e.*, $k_r = k_t = \infty$) and web single curvature bending – therefore, it does not capture the buckling mode shapes of beams B0-250-1.6 and B0-2500-4.5, displayed in Fig. 22.

(vi) Although Zhou's model (Zhou *et al.* 2016) is able to capture S-LDB and D-LDB (*e.g.*, beams B-2500-2.5 and B-2500-5.0 in Fig. 22), it also assumes a fully restrained top flange. Thus, errors below 10% are only achieved in beams buckling in LDB mode with very small (almost null) top flange rotation – thus, it does not capture the buckling mode shapes of beams B-250-2.5 and B-500-4.5, shown in Fig. 22.

(vii) The buckling moments yielded by the SFEA and the Hanswille's (Hanswille *et al.* 1998) and Dias' (Dias *et al.* 2019) models virtually coincide for the beams exhibiting S-LDB (differences below 3.5% – *e.g.*, beams B-250-2.5 and B-2500-2.5). Conversely, the buckling moments of beams exhibiting D-LDB differ considerably, since errors range from 15% (beam B-500-4.5) to 30% (beam B-2500-5.0).

(viii) Although the presence of web double curvature in the buckling mode shape may be barely perceptible to the naked eye (see Fig. 22), neglecting it can lead to unsafe designs of I-section steel beams restrained by concrete slabs, even for cross-sections with $t_f /t_w \leq 4$.

---

[10] In the ANSYS SFEA, the beams are discretised by means of refined meshes of SHELL181 elements (ANSYS nomenclature: isoparametric 4-node shell elements), employed with the "full integration" option – 32 elements were considered along the cross-section mid-line (16 in the web and 8 per flange) and previous convergence studies showed that an element length-to-width ratio comprised between 1.0 and 2.0 leads to accurate results.

Table 2: Restrained I-section beams (b_w=600mm, b_f=200mm, t_w=12.5mm) with L=7 m: LDB moments obtained by GBT-based formulae, ANSYS and other analytical formulae

Model	t_f (mm)	A_s (cm²/m)	$\bar{y}$ (cm)	N_x (kN)	M_z (kN.m)	k_z (kNcm/rad/cm)	ANSYS (2013) $M_{cr.Shell}$ (kN.m)	Silvestre (2010) $M_{cr.S}$ (kN.m)	$\frac{M_{cr.S}}{M_{cr.Shell}}$	Hanswille et al. (1998) $M_{cr.H}$ (kN.m)	$\frac{M_{cr.H}}{M_{cr.Shell}}$	Zhou et al. (2016) $M_{cr.Z}$ (kN.m)	$\frac{M_{cr.Z}}{M_{cr.Shell}}$	Dias et al. (2019) $M_{cr.D}$ (kN.m)	$\frac{M_{cr.D}}{M_{cr.Shell}}$	GBT Analytical Formula Eq. (51) M_{cr} (kN.m)	$\frac{M_{cr}}{M_{cr.Shell}}$	Modal Participation Eq. (56) MP_{LD} (%)	MP_L (%)	η	Buckling Mode
B0-250-1.6						250	1237.5	1565.6	1.27	1241.8	1.00	1519.4	1.23	1241.8	1.00	1245.4	1.01	99.8	0.2	1	S-LDB
B0-500-1.6	16					500	1419.6	1565.6	1.10	1428.6	1.01	1519.4	1.07	1428.6	1.01	1430.2	1.01	99.1	0.9	2	S-LDB
B0-2500-1.6						2500	1508.3	1565.6	1.04	1501.4	1.00	1519.4	1.01	1501.4	1.00	1520.2	1.01	99.1	0.9	2	S-LDB
B0-250-2.5						250	1531.4	2256.8	1.47	1583.9	1.03	2176.8	1.42	1583.9	1.03	1551.0	1.01	98.9	1.1	1	S-LDB
B0-500-2.5	25					500	1772.4	2256.8	1.27	1811.2	1.02	2176.8	1.23	1811.2	1.02	1793.0	1.01	98.9	1.1	1	S-LDB
B0-2500-2.5		0	0	0	1	2500	2095.0	2256.8	1.08	2102.4	1.00	2176.8	1.04	2102.4	1.00	2118.4	1.01	98.9	1.1	1	S-LDB
B0-250-4.5						250	2649.4	4005.0	1.51	3196.8	1.21	3439.9	1.30	3196.8	1.21	2726.0	1.03	89.9	10.1	1	D-LDB
B0-500-4.5	45					500	2903.7	4005.0	1.38	3424.1	1.18	3439.9	1.18	3424.1	1.18	2957.7	1.02	89.0	11.0	1	D-LDB
B0-2500-4.5						2500	3301.8	4005.0	1.21	3715.2	1.13	3439.9	1.04	3715.2	1.13	3346.2	1.01	88.6	11.4	1	D-LDB
B0-250-5.0						250	2963.8	4730.0	1.60	3856.4	1.30	3817.1	1.29	3856.4	1.30	3109.7	1.05	86.5	13.5	1	D-LDB
B0-500-5.0	50					500	3230.3	4730.0	1.46	4083.7	1.26	3817.1	1.18	4083.7	1.26	3316.3	1.03	85.1	14.9	1	D-LDB
B0-2500-5.0						2500	3644.6	4730.0	1.30	4374.9	1.20	3817.1	1.05	4374.9	1.20	3711.6	1.02	84.5	15.5	1	D-LDB
B-250-1.6						250	1406.5	-	-	1401.3	1.00	1706.1	1.21	1435.5	1.02	1415.0	1.01	99.7	0.3	1	S-LDB
B-500-1.6	16		4.939	0.6296	0.7346	500	1615.0	-	-	1612.1	1.00	1706.1	1.06	1651.4	1.02	1626.9	1.01	98.9	1.1	2	S-LDB
B-2500-1.6						2500	1721.6	-	-	1694.2	0.98	1706.1	0.99	1735.5	1.01	1735.1	1.01	98.9	1.1	2	S-LDB
B-250-2.5						250	1682.3	-	-	1737.8	1.03	2373.6	1.41	1755.5	1.04	1703.3	1.01	98.8	1.2	1	S-LDB
B-500-2.5	25		4.063	0.4978	0.7879	500	1950.5	-	-	1987.2	1.02	2373.6	1.22	2007.5	1.03	1972.6	1.01	98.8	1.2	1	S-LDB
B-2500-2.5		18.45				2500	2310.6	-	-	2306.6	1.00	2373.6	1.03	2330.1	1.01	2335.4	1.01	98.8	1.2	1	S-LDB
B-250-4.5						250	2812.6	-	-	3412.1	1.21	3645.8	1.30	3407.9	1.21	2894.3	1.03	89.8	10.2	1	D-LDB
B-500-4.5	45		2.942	0.3449	0.8496	500	3085.9	-	-	3654.7	1.18	3645.8	1.18	3650.3	1.18	3143.5	1.02	88.8	11.2	1	D-LDB
B-2500-4.5						2500	3512.5	-	-	3965.4	1.13	3645.8	1.04	3960.6	1.13	3560.5	1.01	88.5	11.5	1	D-LDB
B-250-5.0						250	3133.0	-	-	4100.6	1.31	4029.5	1.29	4090.0	1.31	3286.4	1.05	86.4	13.6	1	D-LDB
B-500-5.0	50		2.757	0.3210	0.8592	500	3416.0	-	-	4342.3	1.27	4029.5	1.18	4331.1	1.27	3507.8	1.03	85.0	15.0	1	D-LDB
B-2500-5.0						2500	3857.4	-	-	4651.8	1.21	4029.5	1.04	4639.8	1.20	3930.1	1.02	84.5	15.5	1	D-LDB
Mean								Mean	1.31	Mean	1.11	Mean	1.17	Mean	1.12	Mean	**1.02**				
Sd.dev.								Sd.dev.	0.18	Sd.dev.	0.11	Sd.dev.	0.13	Sd.dev.	0.11	Sd.dev.	**0.01**				

B0-250-1.6	B0-2500-4.5	B-250-2.5	B-2500-2.5	B-500-4.5	B-2500-5.0
S-LDB	D-LDB	S-LDB	S-LDB	D-LDB	D-LDB

GBT-based analytical formulae
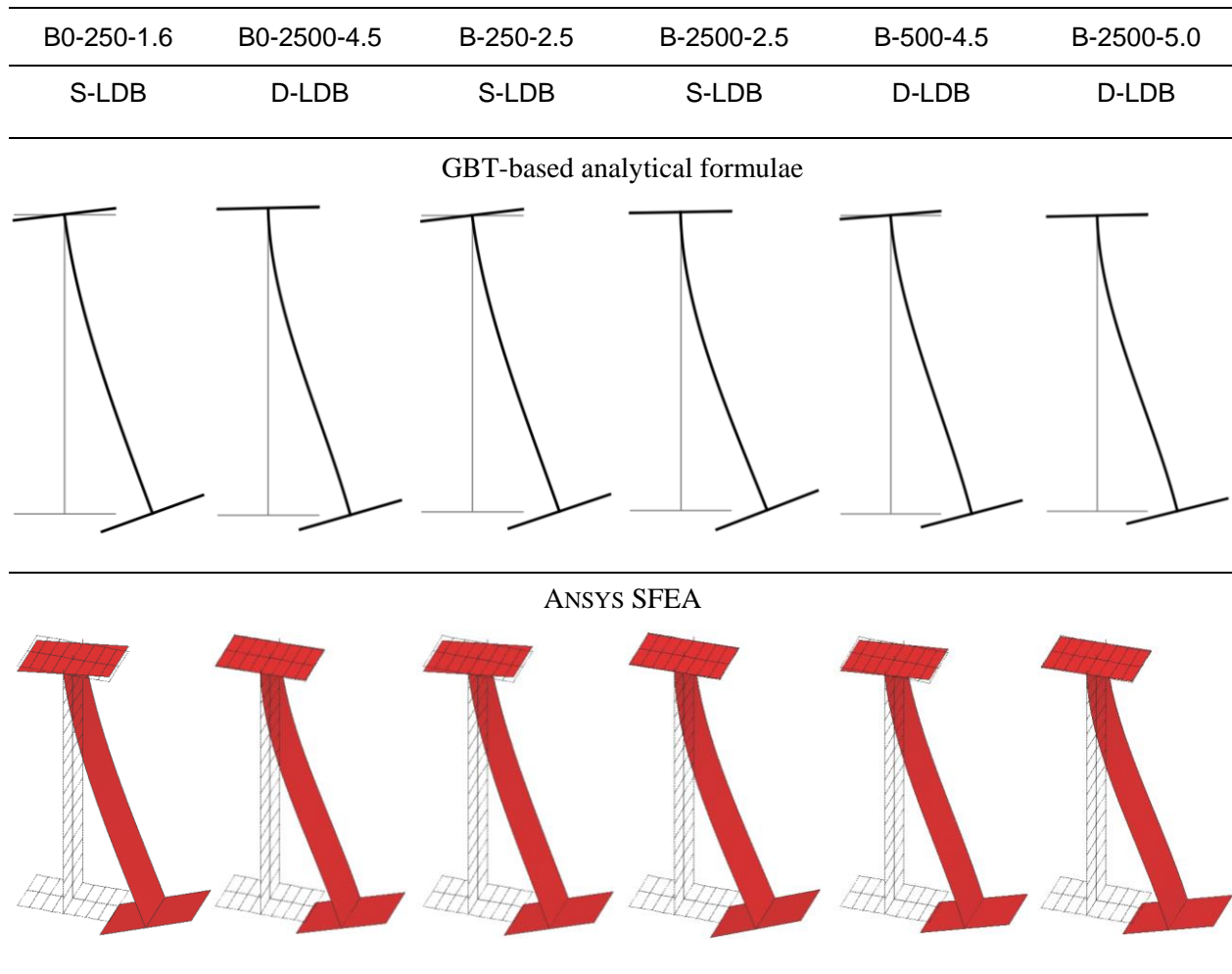
ANSYS SFEA

Figure 22: Critical buckling mode shapes obtained by GBT-based analytical formulae and ANSYS SFEA

5. Conclusion

This paper dealt with the derivation of an improved constrained-mode GBT-based approach, intended (i) to shed fresh light on the kinematics and mechanics of (web) single and double curvature LDB in I-section steel beams elastically restrained by concrete slabs, and also (ii) to enable the development of accurate analytical formulae to the calculate critical moments associated with these buckling phenomena.

After deriving the GBT equilibrium equation system incorporating the elastic restraints/springs, the main concepts and procedures involved in determining the constrained deformation modes of open "branched" cross-sections were described and illustrated. Next, in order to clarify some behavioral features associated with the LDB of I-section steel beams elastically restrained by concrete slabs, results concerning the constrained-mode GBT buckling analyses of simply supported beams under uniform hogging bending moments were presented and discussed. For validation and assessment purposes, several results obtained with the proposed GBT-based approach were compared with values yielded by the programs GBTUL2.0 (conventional GBT) and CUFSM (finite strip method) – an excellent agreement was invariably found.

Finally, it was shown that using the decomposition of the GBT-based buckling solution, into constrained lateral-distortional and local deformation modes, made it possible (i) to obtain in-depth insight into the mechanics underlying LDB, (ii) obtain simplified (but accurate) expressions for the lateral-distortional displacement field and (iii) derive analytical formulae providing critical buckling moment estimates. For validation and accuracy assessment purposes, these estimates were compared with "exact values" yielded by either conventional GBT or shell finite element analyses – an excellent performance was found in all cases. Moreover, critical buckling moment estimates obtained in this work were shown to compare favorably, both in accuracy and scope, with those provided by other analytical formulae available in the literature.

Out of the various features of the proposed GBT-based approach to analyses the buckling behavior of restrained members open "branched" cross-sections, the following ones deserve to be highlighted:

(i)   It mechanically more illuminating than the conventional GBT approach. In particular, it is possible to obtain accurate buckling results with less deformation modes (often with just one or two).

(ii)   The constrained deformation modes provide insightful information about the restrained I-section beam mechanics – this GBT feature was crucial for the accurate determination of the lateral-distortional deformation field, as well as to acquire an in-depth understanding of the associated kinematics.

(iii)   Enabled the derivation of analytical formulae were to estimate critical S-LDB and D-LDB moments of I-section steel beams elastically restrained by concrete slabs – such formulae were found to consistently yield accurate critical buckling moment estimates (in the overwhelming majority of the cases analysed, the error did not exceed 1.2%). Moreover, the constrained modal decomposition of the beam critical S-LDB or D-LDB mode shapes (**LD** and **L** modal participations) provide insightful information on their mechanical nature.

(iv)   Neglecting the web double curvature my lead to unsafe designs of I-section steel beams restrained by concrete slabs under uniform hogging bending moments, even in thick-flange cross-sections ($t_f/t_w \leq 4$).

Acknowledgments

References

Amaral TV, Oliveira JPS, Calenzani AFG, Teixeira FB (2018). Lateral-distortional buckling of continuous steel-concrete composite beam, *Ibracon Structures and Materials Journal*, **11**(4), 719-756.

Araujo HF, Basaglia C, Camotim D da Silva TG. (2021). Improving the GBT-based buckling analysis of restrained cold-formed steel members by considering constrained deformation modes, *Thin-Walled Structures*, **165**(August), paper 107928 (33 pages).

Basaglia C, Camotim D (2013). Enhanced generalised beam theory buckling formulation to handle transverse load application effects, *International Journal of Solids and Structures*, **50**(3-4), 531-547.

Bebiano R, Gonçalves R, Camotim D (2015). A cross-section analysis procedure to rationalise and automate the performance of GBT-based structural analyses, *Thin Walled Structures*, **92**(July), 29-47.

Bebiano R, Camotim D, Gonçalves R (2018). GBTUL 2.0 − A second-generation code for the GBT-based buckling and vibration analysis of thin-walled members, *Thin Walled Structures*, **124** (March), 235-257.

Bradford MA (1986). Inelastic distortional buckling of I-beams, *Computers & Structures*, **24**(6), 923-933.

Bradford MA (1988). Buckling of elastically restrained beams with web distortions, *Thin-Walled Structures*, **6**(4), 287-304.

Bradford MA (1988). Buckling strength of deformable monosymmetric I-beams, *Engineering Structures*, **10**(3), 167-173.

Bradford MA (1992). Lateral-distortional buckling of steel I-section members, *Journal of Constructional Steel Research*, **23**(1-3), 97-116.

Bradford MA (1998). Distortional buckling of elastically restrained cantilevers, *Journal of Constructional Steel Research*, **47**(1-2), 3-18.

Bradford MA (1998). Inelastic buckling of I-beams with continuous elastic tension flange restraint, *Journal of Constructional Steel Research*, **48**(2-3), 63-67.

Calenzani AFG, Fakury RH, de Paula FA, Rodrigues FC, Queiroz G, Pimenta RJ (2012). Rotational stiffness of continuous composite beams with sinusoidal-web profiles for lateral-torsional buckling, *Journal of Constructional Steel Research*, **79**(December), 22-33.

Camotim D, Basaglia C (2013). Buckling analysis of thin-walled structures using Generalised Beam Theory (GBT): state-of-the-art report, *Steel Construction*, **6**(2), 117-131.

Camotim D, Silvestre N, Basaglia C, Bebiano R (2008). GBT-based buckling analysis of thin-walled members with non-standard support conditions, *Thin Walled Structures*, **46**(7-9), 800-815.

Comité Européen de Normalisation (CEN) (2004). *Eurocode 4 – Design of Steel Structures – Part 1-1: General Rules and Rules for Buildings*, EN1993-1-1, Brussels.

Dias JVF, Oliveira JPS, Calenzani AFG, Fakury RH (2019). Elastic critical moment of lateral-distortional buckling of steel-concrete composite beams under uniform hogging moment, *International Journal of Structural and Dynamics*, **19**(7), paper 1950079 (17 pages).

Dietrich MZ, Calenzani AFG, Fakury RH (2019). Analysis of rotational stiffness of steel-concrete composite beams for lateral-torsional buckling, *Engineering Structures*, **198**(November), paper 109554 (15 pages).

Dinis PB, Camotim D, Silvestre N (2006). GBT formulation to analyse the buckling behaviour of thin-walled members with arbitrarily "branched" open cross-sections, *Thin Walled Structures*, **44**(1), 20-38.

Goltermann P, Svensson SE (1988). Lateral distortional buckling: predicting elastic critical stress, *Journal of Structural Engineering* (ASCE), **114**(7), 1606-1625.

Gonçalves R, Camotim D (2010). Steel-concrete composite bridge analysis using generalised beam theory, *Steel and Composite Structures*, **10**(3), 223-243.

Hanswille G, Lindner J, Münich D (1998). Zum Biegedrillknicken von Verbundträgern, *Stahlbau*, **67**(7), 525-535. (German)

Henriques D, Gonçalves R, Camotim D (2016). GBT-based finite element to assess the buckling behaviour of steel-concrete composite beams, *Thin-Walled Structures*, **107**(October), 207-220.

Henriques D, Gonçalves R, Sousa C, Camotim D (2020). GBT-based time-dependent analysis of steel-concrete composite beams including shear lag and concrete cracking effects, *Thin-Walled Structures*, **120**(May), paper 106706 (17 pages).

Johnson RP, Fan CKR (1991). Distortional lateral buckling of continuous composite beams, *Proceedings of the Institution of Civil Engineers*, **91**(1), 131-161.

Li Z, Schafer BW (2010). Application of the finite strip method in cold-formed steel member design, *Journal of Constructional Steel Research*, **66**(8-9), 971-980.

Reddy JN (2006). *An Introduction to the Finite Element Method* (3rd ed.), McGraw-Hill, New York.

Rossi A, Nicoletti RS, de Souza ASC, Martins CH (2020). Lateral distortional buckling in steel-concrete composite beams: a review, *Structures*, **27**(October), 1299-1312.

SAS (Swanson Analysis Systems Inc.) (2013). *ANSYS Reference Manual* (version 15).

Schardt R. (1989). *Verallgemeinerte Technische Biegetheorie*, Springer-Verlag, Berlin. (German)

Silvestre N (2010). Distortional mechanics of restrained steel sections, *Journal of Constructional Steel Research*, **66**(7), 873-884.

Silvestre N, Camotim D (2002). First-order generalised beam theory for arbitrary orthotropic materials, *Thin Walled Structures*, **40**(9), 755-789.

Silvestre N, Camotim D (2003). GBT buckling analysis of pultruded FRP lipped channel members, *Computers and Structures*, **81**(18-19), 1889-1904.

Silvestre N, Camotim D (2004). Distortional buckling formulae for cold-formed steel C and Z-section members: Part I – derivation, *Thin Walled Structures*, **42**(11), 1567-1597.

Silvestre N, Camotim D (2004). Distortional buckling formulae for cold-formed steel C and Z-section members: Part II – validation and application, *Thin Walled Structures*, **42**(11), 1599-1629.

Silvestre N, Camotim D (2004). Distortional buckling formulae for cold-formed steel rack-section members, *Steel & Composite Structures*, **4**(1), 49-75.

Silvestre N, Camotim D (2010). On the mechanics of distortion in thin-walled open section, *Thin Walled Structures*, **48**(7), 469-481.

Vayas I, Iliopoulos A (2014). *Design of Steel-Concrete Composite Bridges to Eurocodes*, CRS Press, Boca Raton.

Zhou W-B, Li S-J, Yan W-J (2016). Practical formulas towards distortional buckling failure analysis for steel-concrete composite beams, *The Structural Design of Tall and Special Buildings*, **25**(18), 1055-1072.

Zhou W-B, Yan W-J (2017). Refined nonlinear finite element modelling towards ultimate bending moment calculation for concrete composite beams under negative moment, *Thin-Walled Structures*, **116**(July), 201-211.